

LAL/99-06

A NEW GLOBAL ANALYSIS OF DEEP INELASTIC SCATTERING DATA

V. Barone^{a,b}, C. Pascaud^c and F. Zomer^c

^a Dipartimento di Fisica Teorica, Università di Torino
and INFN, Sezione di Torino, via P. Giuria 1, I-10125, Torino, Italy

^b D.S.T.A., Università “A. Avogadro”,

c.so Borsalino 54, I-13100 Alessandria, Italy

^c Laboratoire de l’Accélérateur Linéaire, IN2P3-CNRS
and Université de Paris-Sud, F-91898 B.P. 34 Orsay Cedex, France

Abstract

A new QCD analysis of Deep Inelastic Scattering (DIS) data is presented. All available neutrino and anti-neutrino cross sections are reanalysed and included in the fit, along with charged-lepton DIS and Drell-Yan data. A massive factorisation scheme is used to describe the charm component of the structure functions. Next-to-leading order parton distribution functions are provided. In particular, the strange sea density is determined with a higher accuracy with respect to other global fits.

1 Introduction

In Deep Inelastic Scattering (DIS) processes a neutral or charged lepton ℓ interacts with a nucleon N yielding a lepton ℓ' and a set of undetected hadrons X in the final state. The kinematics of this process, $\ell(k) + N(p) \rightarrow \ell'(k') + X$, is determined by two independent variables, besides the energy of the incoming lepton. One usually chooses them among the four Lorentz invariants

$$Q^2 \equiv -q^2 = -(k - k')^2, \quad x = \frac{Q^2}{2p \cdot q}, \quad y = \frac{p \cdot q}{p \cdot k}, \quad W^2 = (q + p)^2,$$

which are obtained experimentally by measuring the momentum, the direction of the scattered lepton and the initial momenta k, p .

Studies of DIS processes, both on the experimental [1] and on the theoretical side [2], have shed light on the nucleon internal dynamics. In particular, powerful tests of perturbative Quantum Chromo Dynamics (pQCD) have been carried out, consisting of global analyses performed on a large class of DIS observables. Among these the structure functions measured in neutrino (anti-neutrino) DIS play a major role for the determination of the flavour distributions, in particular the valence and the strange sea densities.

What experiments directly measure is a differential cross-section from which the structure functions are extracted by means of a theoretical analysis. This includes the application of electroweak radiative corrections, the determination of $R = \sigma_L/\sigma_T$, the incorporation of possible nuclear effects, etc ... In particular, the analysis of neutrino data is a difficult and delicate procedure (see [3] for a clear and detailed description), and so far only a small part of the information accumulated in $\nu(\bar{\nu})$ DIS has been exploited in the QCD parametrisations.

The purpose of this paper is to present a new global analysis of DIS data which includes the available ν and $\bar{\nu}$ cross section measurements¹, besides the structure function data collected in charged-lepton DIS experiments. We resort directly to the $\nu(\bar{\nu})$ DIS differential cross sections, avoiding to use the neutrino structure function results. The latter are the product of a preanalysis which may be (and often indeed is) based on theoretical assumptions different from those of the global fit that one is performing. Thus, for a full consistency, we use only *cross section* data. This limits our neutrino (and anti-neutrino) data set to the BEBC (Hydrogen target) [5], CDHS (Hydrogen and Deuterium targets) [6] and CDHSW (Iron target) [7] measurements. The CHARM [8] and CCFR [9] experiments do not provide cross sections but only structure functions and hence their results are not included in our analysis.

The problem with the BEBC, CDHS and CDHSW data is that they cannot be used in the form they were published, since the electroweak radiative corrections were either incomplete or not applied at all and/or the bin centre corrections were

¹This type of analysis was proposed long ago by M.W. Krasny [4].

not performed. Thus we had to reevaluate the neutrino cross sections to take all these corrections into account. This is the preliminary step of our analysis. Since most of the ν ($\bar{\nu}$) DIS data come from nuclear targets, nuclear corrections must also be applied.

Besides the neutrino data, the structure function measurements from charged-lepton DIS experiments (NMC [10], BCDMS [11], H1 [12]) are included in our fits. The only non DIS data we use are the Drell–Yan [13, 14, 15] data which constrain the light sea.

Our fitting procedure is designed in such a way to take properly into account the experimental uncertainties and the correlations among them, which are known to affect the Q^2 slopes of the structure functions and ultimately the determination of the parton densities [16].

An important feature of the QCD analysis presented in this paper is the accurate treatment of the charm contribution to the structure functions. A massive factorisation scheme is used, the so-called Fixed Flavour Scheme [17]. It is known [18] that for a precise extraction of the strange sea density, charm mass effects cannot be neglected and have to be correctly incorporated.

In extracting the parton distributions, the neutrino data (in particular the high-statistics CDHSW data) add a great quantity of information to that coming from charged-lepton DIS. The latter is insufficient to constrain all flavour distributions, being essentially limited to one observable, F_2 . Charged-current DIS provides four more independent combinations of parton densities, F_2^ν , $F_2^{\bar{\nu}}$, xF_3^ν , $xF_3^{\bar{\nu}}$. As a consequence, the abundance of neutrino data in our fit ensures an excellent accuracy in the determination of the flavour densities.

A special emphasis will be given to the strange sea density. Due to the lack of data able to constrain it, in the existing fits [19, 20] this distribution is tightly related to the non-strange sea distributions and essentially borrowed² from the CCFR extraction [22]. Clearly, this is not a consistent procedure. Here we present the first fully consistent determination of the strange distribution within a global fit of all parton densities. The wealth of neutrino and anti-neutrino data will also allow us to test the possible charge asymmetry of the strange sea ($s \neq \bar{s}$) predicted by some authors.

In the present work the strong coupling constant is independently fixed to a value close to the world average. In a forthcoming paper we shall study the possibility of determining α_s from the minimisation of the total χ^2 of the fit, and discuss the stability of this determination and its correlation with the gluon density.

The article is organised as follows. In section 2 we collect the main theoretical ingredients of the QCD analysis of DIS data. The re-evaluation of the neutrino and anti-neutrino differential cross sections is the content of section 3. The fitting

²In the GRV fit [21] the strange distribution is assumed to be zero at a very low Q^2 scale and then entirely generated by the QCD evolution.

procedure is described in section 4. Finally, the results on cross sections, structure functions and parton distribution functions are presented in section 5.

2 Deep inelastic scattering in QCD

The differential cross section of neutral-current (NC) DIS of charged leptons (ℓ), in the one-boson approximation and for moderate $Q^2 \ll M_Z^2$, is given by

$$\frac{d^2\sigma^{\ell N}}{dxdy} = \frac{8\pi\alpha_{em}^2 M_N E}{Q^2} \left[xy^2 F_1^{\ell N}(x, Q^2) + \left(1 - y - \frac{M_N xy}{2E}\right) F_2^{\ell N}(x, Q^2) \right], \quad (1)$$

If $Q^2 \ll M_Z^2$ charged-lepton NC DIS is essentially an electromagnetic reaction (that is dominated by one-photon exchange), the Z^0 contribution being totally negligible. In eq. (1) $\alpha_{em} = 1/137$ is the electromagnetic coupling constant, E is the beam energy and M_N is the nucleon mass.

For charged-current (CC) neutrino (anti-neutrino) DIS one has

$$\begin{aligned} \frac{d^2\sigma^{\nu(\bar{\nu})N}}{dxdy} &= \frac{G_F^2 M_N E}{\pi} \left(\frac{M_W^2}{Q^2 + M_W^2} \right)^2 \\ &\times \left[xy^2 F_1^{\nu(\bar{\nu})N}(x, Q^2) + \left(1 - y - \frac{M_N xy}{2E}\right) F_2^{\nu(\bar{\nu})N}(x, Q^2) \right. \\ &\left. + (-) \left(y - \frac{y^2}{2} \right) x F_3^{\nu(\bar{\nu})N}(x, Q^2) \right], \end{aligned} \quad (2)$$

where M_W is W -boson mass and G_F is the Fermi coupling constant.

In QCD the structure functions F_2 , $F_L = F_2 - 2xF_1$ and xF_3 are given by the convolution of the parton distribution functions (pdf's) with some perturbatively calculable coefficient functions. In the kinematic range covered by the analysis presented in this article the contribution of the b quark is negligible and the only heavy quark considered is charm. Therefore we split the structure functions in two components

$$F_i(x, Q^2) = F_{i,l}(x, Q^2) + F_{i,c}(x, Q^2), \quad i = 2, 3, L$$

where $F_{i,l}(x, Q^2)$ is the light-parton contribution and $F_{i,c}(x, Q^2)$ is the charm contribution. In the CC case the latter mixes charm with light quarks.

The massive scheme that we adopt is the Fixed Flavour Scheme (FFS) [17] in which charm is a ‘heavy’ quark in absolute sense. This means that there is no such thing as the charm density function and charm is radiatively produced. Consequently the number of active flavours is set to 3 irrespective of Q^2 . The FFS has been shown to be more stable than the alternative massive scheme, the Variable Flavour Scheme (VFS) [23], at moderate Q^2 where most of the neutrino data lie [24, 25].

| | $F_{2,l}$ | $F_{2,c}$ |
|---------------|--|---|
| $\ell^\pm p$ | $x[\frac{4}{9}(u + \bar{u}) + \frac{1}{9}(d + \bar{d} + s + \bar{s})]$ | $\frac{4}{9}(\frac{\alpha_s}{2\pi}) C_{2,g}^{c,(0)} \otimes xg$ |
| $\ell^\pm n$ | $x[\frac{4}{9}(d + \bar{d}) + \frac{1}{9}(u + \bar{u} + s + \bar{s})]$ | $\frac{4}{9}(\frac{\alpha_s}{2\pi}) C_{2,g}^{c,(0)} \otimes xg$ |
| νp | $2x[\bar{u} + d V_{ud} ^2 + s V_{us} ^2]$ | $2\xi[d(\xi) V_{cd} ^2 + s(\xi) V_{cs} ^2]$ |
| νn | $2x[\bar{d} + u V_{ud} ^2 + s V_{us} ^2]$ | $2\xi[u(\xi) V_{cd} ^2 + s(\xi) V_{cs} ^2]$ |
| $\bar{\nu} p$ | $2x[u + \bar{d} V_{ud} ^2 + \bar{s} V_{us} ^2]$ | $2\xi[\bar{d}(\xi) V_{cd} ^2 + \bar{s}(\xi) V_{cs} ^2]$ |
| $\bar{\nu} n$ | $2x[d + \bar{u} V_{ud} ^2 + \bar{s} V_{us} ^2]$ | $2\xi[\bar{u}(\xi) V_{cd} ^2 + \bar{s}(\xi) V_{cs} ^2]$ |

Table 1: Leading-order expressions of F_2 (l : light sector; c : charm sector in the FFS). The x and Q^2 arguments have been omitted. Only the slow-rescaled argument ξ has been explicitly indicated.

| | $xF_{3,l}$ | $xF_{3,c}$ |
|---------------|---|--|
| νp | $2x[d V_{ud} ^2 + s V_{us} ^2 - \bar{u}]$ | $2\xi[d(\xi) V_{cd} ^2 + s(\xi) V_{cs} ^2]$ |
| νn | $2x[u V_{ud} ^2 + s V_{us} ^2 - \bar{d}]$ | $2\xi[u(\xi) V_{cd} ^2 + s(\xi) V_{cs} ^2]$ |
| $\bar{\nu} p$ | $2x[u - \bar{d} V_{ud} ^2 - \bar{s} V_{us} ^2]$ | $-2\xi[\bar{d}(\xi) V_{cd} ^2 + \bar{s}(\xi) V_{cs} ^2]$ |
| $\bar{\nu} n$ | $2x[d - \bar{u} V_{ud} ^2 - \bar{s} V_{us} ^2]$ | $-2\xi[\bar{u}(\xi) V_{cd} ^2 + \bar{s}(\xi) V_{cs} ^2]$ |

Table 2: Same as table 1, for xF_3 .

In the strong coupling, heavy quark thresholds are accounted for according to the prescription of Ref. [26] (with $m_c = 1.5$ GeV and $m_b = 4$ GeV).

The leading-order (LO) expressions for F_2 and xF_3 are collected in Tables 1 and 2. Note that:

- $\xi = x(1 + Q^2/m_c^2)$ is the slow-rescaling variable; $m_c = 1.5$ GeV is the charm mass.
- V_{ij} are the Cabibbo-Kobayashi-Maskawa matrix elements. We shall use $|V_{us}| = |V_{cd}| = 0.224$ and $|V_{ud}| = |V_{cs}| = \sqrt{1 - |V_{us}|^2}$.
- The symbol \otimes stands for convolution:

$$f \otimes g = \int_{ax}^1 \frac{dz}{z} f(z) g(x/z),$$

where $a = 1$ for the light sector, $a = 1 + 4m_c^2/Q^2$ for NC charm production, $a = 1 + m_c^2/Q^2$ for CC charm production.

- The LO charm contribution to F_2 in the neutral-current charged-lepton case is a $\mathcal{O}(\alpha_s)$ quantity in the Fixed Flavour Scheme. $C_{2,g}^{c,(0)}$ is the LO Wilson coefficient for the photon-gluon fusion process [27]. Explicitly:

$$F_{2,c}^{\ell N}(x, Q^2) = \frac{4}{9} \left(\frac{\alpha_s}{2\pi} \right) C_{2,g}^{c,(0)}(m_c^2/Q^2) \otimes xg(\mu^2), \quad (3)$$

where the strong coupling is evaluated at the factorisation scale μ , and $C_{2,g}^{c,(0)}(z, m_c^2/Q^2)$ can be found for instance in [17].

- The charm production is different in neutral and charged current DIS. In the former case it is given at LO by gluon splitting into a $c\bar{c}$ pair. In the latter case it is given by the direct process $W^+s \rightarrow c$, with the slow-rescaling variable taking into account the effect of the charm mass.
- At order α_s^0 the longitudinal structure function $F_L = F_2 - 2xF_1$ vanishes.

The QCD analysis performed in this paper is at the next-to-leading order (NLO) level (the renormalization scheme adopted is \overline{MS}). NLO means $\mathcal{O}(\alpha_s)$ for the light sector and for the charm contribution to CC DIS, $\mathcal{O}(\alpha_s^2)$ for the charm contribution to NC DIS in the Fixed Flavour Scheme. Since F_L vanishes at order α_s^0 , for consistency with the treatment of the charm structure function, we include in our NLO analysis the order α_s^2 contribution to F_L , except for the strange-charm component of F_L , for which the $\mathcal{O}(\alpha_s^2)$ longitudinal Wilson coefficients are not known yet. Anyway, this contribution has a very little effect in the kinematic domain of our analysis.

The light-parton components of the structure functions have the form (for illustration we write only F_2 for the electromagnetic case):

$$F_{2,l}^{\ell N}(x, Q^2) = \sum_{f=q, \bar{q}} e_f^2 \left\{ \left(1 + \frac{\alpha_s}{2\pi} C_{2,f}^{(1)} \right) \otimes xf + \frac{\alpha_s}{2\pi} C_{2,g}^{(1)} \otimes xg \right\}. \quad (4)$$

The \overline{MS} Wilson coefficients $C_{i,q}^{(1)}$ and $C_{i,g}^{(1)}$ with $i = 2, 3, L$ can be found in Appendix I of Ref. [28]. As mentioned above, for $F_{L,l}$ we consider also the $\mathcal{O}(\alpha_s^2)$ contributions to the coefficient functions calculated in Ref. [29]³.

The parton densities xf and xg are obtained by solving the DGLAP equations at NLO [30]. For the light sector we choose $\sqrt{Q^2}$ as the factorisation and renormalisation scale.

The NLO expression of the charm contribution to the NC structure functions is

$$\begin{aligned} F_{2,c}^{\ell N}(x, Q^2) = & \frac{\alpha_s}{2\pi} \left\{ \frac{4}{9} \left[C_{2,g}^{c,(0)}(m_c^2/Q^2) + \frac{\alpha_s}{2\pi} C_{2,g}^{c,(1)}(m_c^2/Q^2) \right] \otimes xg(\mu^2) \right. \\ & + \frac{\alpha_s^2}{(2\pi)^2} \sum_{f=q, \bar{q}} \left[\frac{4}{9} C_{2,f}^{c,(1)}(m_c^2/Q^2) \otimes xf(\mu^2) \right. \\ & \left. \left. + e_f^2 D_{2,f}^{c,(1)}(m_c^2/Q^2) \otimes xf(\mu^2) \right] \right\}. \end{aligned} \quad (5)$$

The NLO coefficients $C^{c,(1)}$ and $D^{c,(1)}$ for $F_{2,c}^{\ell N}$ and $F_{L,c}^{\ell N}$ have been computed in the Fixed Flavour Scheme in [31]. For our calculations we have used the tables presented in [32].

The NLO strange-charm component of the structure functions is given by (omitting the Cabibbo-suppressed term and again writing only F_2 for simplicity)

$$F_{2,c}^{\nu N}(x, Q^2) = 2 \left\{ \left(1 + \frac{\alpha_s}{2\pi} H_{2,f}^{c,(1)} \right) \otimes \xi s + \frac{\alpha_s}{2\pi} H_{2,g}^{c,(1)} \otimes \xi g \right\}, \quad (6)$$

The Wilson coefficients $H_{i,f}^{c,(1)}$ and $H_{i,g}^{c,(1)}$ ($i = 2, 3, L$) have been computed in [33] and can be found, with a convention update, also in [34, 35]. The factorisation and renormalisation scale for the charm structure functions is chosen to be $\sqrt{Q^2 + m_c^2}$.

3 Re-evaluation of neutrino cross sections

3.1 Bin centre and radiative corrections

We start with a general description of the procedure of bin centre and electroweak radiative corrections. We shall then give the details of the application of this procedure to the various data sets.

³We thank W. van Neerven for having provided us the code which computes the order α_s^2 Wilson coefficients of F_L .

The neutrino DIS cross-sections are determined experimentally in bins of three kinematic variables, say (x, y, E) . The total cross section σ_{ijk}^{tot} corresponding to the bin $[x_i, x_{i+1}]$, $[y_j, y_{j+1}]$ and $[E_k, E_{k+1}]$ is given by

$$\begin{aligned}\sigma_{ijk}^{tot} &\equiv \int_{x_i}^{x_{i+1}} \int_{y_j}^{y_{j+1}} \int_{E_k}^{E_{k+1}} \frac{d\phi}{dE} \frac{d^2\sigma}{dxdy} dE dx dy \\ &= \frac{N_{ijk}}{C}\end{aligned}\quad (7)$$

where C is the number of scattering centres, N_{ijk} is the number of events corrected for detector effects and background contamination observed in the bin (i, j, k) , $d\phi/dE$ is the neutrino beam energy flux.

In order to relate σ_{ijk}^{tot} to the differential cross section, we invoke the average theorem: there exists at least one point $(\bar{x}_i, \bar{y}_j, \bar{E}_k)$ inside the bin (i, j, k) such that the following relation holds

$$\frac{d^2\sigma(\bar{x}_i, \bar{y}_j, \bar{E}_k)}{dxdy} = \frac{\sigma_{ijk}^{tot}}{S_{ijk}} \quad (8)$$

where $S_{ijk} = \int_{x_i}^{x_{i+1}} \int_{y_j}^{y_{j+1}} \int_{E_k}^{E_{k+1}} \frac{d\phi}{dE} dE dx dy$ is the bin surface.

The differential cross section defined in eq. (8) must be corrected for electroweak radiation effects and translated to the bin centres (x_i^c, y_j^c, E_k^c) . This is done by constructing an “experimental” Born differential cross section defined as

$$\begin{aligned}\frac{d^2\sigma_{exp}^B(x_i^c, y_j^c, E_k^c)}{dxdy} &\equiv \frac{d^2\sigma(\bar{x}_i, \bar{y}_j, \bar{E}_k)}{dxdy} \\ &\times \frac{S_{ijk} d^2\tilde{\sigma}^{B+R}(x_i^c, y_j^c, E_k^c)/dxdy}{\int_{x_i}^{x_{i+1}} \int_{y_j}^{y_{j+1}} \int_{E_k}^{E_{k+1}} \frac{d\phi}{dE} \frac{d^2\tilde{\sigma}^{B+R}}{dxdy} dE dx dy} \\ &\times \frac{d^2\tilde{\sigma}^B(x_i^c, y_j^c, E_k^c)/dxdy}{d^2\tilde{\sigma}^{B+R}(x_i^c, y_j^c, E_k^c)/dxdy}\end{aligned}\quad (9)$$

where the tilde symbol designates the quantities which are theoretically computed, and the upper-scripts $B + R$ and B mean that these calculations are performed including or not, respectively, the higher-order electroweak corrections. The first term on the r.h.s. of eq. (9) is given by eq. (8). The second term embodies the *bin centre corrections* and requires a smooth parametrisation of the data. The third term incorporates the *radiative corrections*.

Combining the last two terms terms we get

$$\frac{d\sigma_{exp}^B(x_i^c, y_j^c, E_k^c)}{dxdy} \equiv \frac{N_{ijk}}{C} \times \frac{d\tilde{\sigma}^B(x_i^c, y_j^c, E_k^c)/dxdy}{\int_{x_i}^{x_{i+1}} \int_{y_j}^{y_{j+1}} \int_{E_k}^{E_{k+1}} \frac{d\phi}{dE} \frac{d^2\tilde{\sigma}^{B+R}(x, y, E)}{dxdy} dE dx dy}. \quad (10)$$

The electroweak corrections to charged current DIS were computed in [36, 37]. In our analysis we used the program of Ref. [38], based on the results of [37]. At

the lowest order radiative corrections include the radiation of virtual and real photons from the charged lepton and quark legs, and the $\gamma - W$ box diagram. We found that these corrections can reach $\sim 20\%$ in some kinematic domains. The correction factor – the third term in eq. (9) – is a ratio, hence it is rather insensitive to QCD corrections [3]. Thus, for simplicity, we computed it at leading order in QCD.

We also evaluated the effects of the higher-order γ radiation from the charged lepton leg [39], using the program HECTOR [40]. This correction typically does not exceed $\sim 0.5\%$ and was applied only to the CDHSW data which are statistically more significant.

3.1.1 CDHSW

The CDHSW Collaboration published [7] the νFe and $\bar{\nu} Fe$ differential cross sections corrected for detector effects and background subtraction. The measurements are binned in x and y for 9 different values of the neutrino beam energies E_k^c between 23 GeV and 187.6 GeV. Neither the bin centre correction in x and y nor the radiative corrections were applied. Thus the full correction of eq. (9) is needed.

To evaluate the correction factors of (9) we cannot use any of the existing parton fits, as they do not account for nuclear effects. Thus we adopt an iterative procedure. In the first step, the bin centre correction and the radiative corrections are determined independently: the former by a parametrisation obtained in two different ways (see below); the latter by a standard fit (we use the LO GRV pdf's [21]). Then, we perform a LO QCD fit to the corrected CDHSW cross sections, to the CDHS data and to the BCDMS, NMC and SLAC [41] structure functions⁴. Using the pdf's of this fit we re-evaluate the full correction factor of eq. (9) and we iterate this step until the corrected differential cross sections get stable. In practice, to achieve the stability only two iterations are required.

As we have mentioned, the smooth parametrisation of the data (required in the bin centre correction) is obtained by two different methods: *i*) by a fit of the CDHSW cross sections (*fitting method*), and *ii*) by an unfolding procedure (*unfolding method*).

In the first method the published CDHSW νFe and $\bar{\nu} Fe$ differential cross section data are fitted to

$$\int_{x_i}^{x_{i+1}} \int_{y_j}^{y_{j+1}} \frac{d^2 \tilde{\sigma}_{\nu(\bar{\nu})}(x, y, E_k^c)}{dxdy} dxdy, \quad k = 1, \dots, 9$$

where $\tilde{\sigma}_{\nu(\bar{\nu})}$ is computed at LO using simple Buras–Gaemers-type pdf's [42] (which incorporate analytically the Q^2 dependence). In parallel we adopted also the unfolding method (described in Appendix I). The difference of the results obtained

⁴Nuclear corrections to neutrino data are applied as explained in section 3.2.

by the two procedures can be taken as a (partial) estimate of the uncertainty on the correction factor applied to neutrino cross sections. We found that after two iterations the results of the two methods are compatible within 1%.

In fig. 1a,b we show the total correction factors applied to the data of the 111 GeV beam sample, as a function of y_j for fixed x_i . They vary between +6% and -4% and are roughly identical for neutrino and anti-neutrino beams. In fig. 1c,d we show the contribution of the electroweak radiative corrections alone, which turns out to be the dominant one.

As for the normalisation of the CDHSW data, in [7] they were normalised using the average total cross sections of [43], namely the ratios $\sigma^{\nu Fe}/E_\nu$ ($\sigma^{\bar{\nu} Fe}/E_{\bar{\nu}}$) were assumed to be independent of the beam energy. This is a strong assumption in view of the fact that a linear rise with the energy is not experimentally excluded [43]. It is therefore important to check the energy dependence⁵.

| \bar{a}_1^ν | \bar{a}_2^ν | $\bar{a}_1^{\bar{\nu}}$ | $\bar{a}_2^{\bar{\nu}}$ |
|---------------------------|-----------------|--------------------------------|-------------------------|
| $(3 \pm 5) \cdot 10^{-4}$ | 0.98 ± 0.05 | $(-2.4 \pm 0.5) \cdot 10^{-5}$ | 1.00 ± 0.04 |

Table 3: Results of the minimisation of χ_ν^2 and $\chi_{\bar{\nu}}^2$. The linear functions of the fits are defined as $\sigma/E = <\sigma/E> (\bar{a}_1 E + \bar{a}_2)$ where $<\sigma/E>$ is the average value (see text). Errors on the parameters are also given.

To this end we performed a linear fit to the measurements $\sigma^{\nu Fe}(E_\nu)/E_\nu$ and $\sigma^{\bar{\nu} Fe}(E_{\bar{\nu}})/E_{\bar{\nu}}$ of [43]. The results, renormalised by the average values $<\sigma^{\nu Fe}/E_\nu> = 0.703 \times 10^{-38} \text{ cm}^2/\text{GeV}$ and $<\sigma^{\bar{\nu} Fe}/E_{\bar{\nu}}> = 0.331 \times 10^{-38} \text{ cm}^2/\text{GeV}$, are given in Table 3 and shown in fig. 2 together with the one-standard-deviation band, computed according to the formulae of Appendix II (we call χ_ν^2 and $\chi_{\bar{\nu}}^2$ the χ^2 's of these fits). A linear rise of $\sigma^{\nu Fe}(E_\nu)/E_\nu$ with E_ν is clearly compatible with the data.

To take into account the effect of the uncertainty of this fit on the CDHSW data, we allow the parameters a_ν and $a_{\bar{\nu}}$ to vary during the global pQCD fit by adding the term

$$\sum_{i,j=1}^2 (a_i^\nu - \bar{a}_i^\nu) M_{ij}^\nu (a_j^\nu - \bar{a}_j^\nu) + (a_i^{\bar{\nu}} - \bar{a}_i^{\bar{\nu}}) M_{ij}^{\bar{\nu}} (a_j^{\bar{\nu}} - \bar{a}_j^{\bar{\nu}}) \quad (11)$$

to the global χ^2 expression. Here \bar{a}_i^ν and $\bar{a}_i^{\bar{\nu}}$ are the parameter values obtained from the preliminary linear fits and the matrices M_{ij}^ν and $M_{ij}^{\bar{\nu}}$ are defined as: $M_{ij}^\nu = (1/2) \partial^2 \chi_\nu^2 / \partial a_i^\nu \partial a_j^\nu$, $M_{ij}^{\bar{\nu}} = (1/2) \partial^2 \chi_{\bar{\nu}}^2 / \partial a_i^{\bar{\nu}} \partial a_j^{\bar{\nu}}$.

Another work done on the CDHSW data is the separation of correlated and uncorrelated systematic errors. The correlated systematic errors are dominated

⁵We thank M.W. Krasny for having suggested to take the energy dependence of the CDHSW data into account in our analysis.

[44] by a possible shift of the hadronic energy by ± 0.5 GeV. As no information has been published, we had to estimate the effects of this uncertainty on the cross-section measurements. In CDHSW, the beam energy E_ν ($E_{\bar{\nu}}$) is experimentally reconstructed [7] via $E_\nu = E_\mu + E_X - M_N$, where E_μ is the measured outgoing muon energy and E_X is the measured hadronic energy in the final state. Thus a shift of the hadronic energy induces a variation of the kinematic variables: $(x, y, Q^2) \rightarrow (x_\pm, y_\pm, Q_\pm^2)$. Our estimate of the relative differential cross section error δ_{ijk}^\pm induced by such shifts is therefore

$$\delta_{ijk}^\pm = \frac{\int_{x_i}^{x_{i+1}} \int_{y_j}^{y_{j+1}} \frac{d^2\tilde{\sigma}^{B+R}(x^\pm, y^\pm, E_k^\pm)}{dxdy} dxdy}{\int_{x_i}^{x_{i+1}} \int_{y_j}^{y_{j+1}} \frac{d^2\tilde{\sigma}^{B+R}(x, y, E)}{dxdy} dxdy}$$

where the cross sections σ^{B+R} are computed as described above. The uncorrelated systematic errors are then obtained by subtracting quadratically the estimated correlated errors from the published systematic errors σ_{ijk}^{syst}

$$\sigma_{ijk}^{uncor} = \sqrt{(\sigma_{ijk}^{syst})^2 - \max(\delta_{ijk}^+, \delta_{ijk}^-)^2}.$$

The treatment of both types of errors in the fit is described in section 4.

Finally, as CDHSW belongs to an old generation of experiments, one may worry about possible sources of errors at high y neglected in their analysis. In particular, one may question two points of the CDHSW analysis (see [3] for more details): *i*) a rejection cut against the dimuon events was used but no correction for it was applied; *ii*) the background coming from muon production in hadronic showers was not taken into account. Using the recent CCFR results on $\sigma_{2\mu}^{\nu, \bar{\nu}} / \sigma_{1\mu}^{\nu, \bar{\nu}}$ [45] and on the production rate of muons in hadronic showers [46], we estimated the effect of these two sources of errors on the measurements and found it to be at the level of 1% at most.

3.1.2 CDHS

The CDHS Collaboration measured [6] the $\nu(\bar{\nu})H$ and $\nu(\bar{\nu})Fe$ differential cross sections. Both the bin centre corrections and the radiative corrections were applied. The latter, however, are incomplete. Only the γ radiation from the muon leg was in fact considered. Hence our first step was to uncorrect back the published CDHS cross sections as follows

$$\frac{d^2\sigma_{uncorr}(x_i^c, y_j^c, E_k^c)}{dxdy} = \frac{d^2\sigma_{publ}(x_i^c, y_j^c, E_k^c)}{dxdy} \cdot \frac{d^2\tilde{\sigma}^{B+\mu}(x_i^c, y_j^c, E_k^c)/dxdy}{d^2\tilde{\sigma}^B(x_i^c, y_j^c, E_k^c)/dxdy}, \quad (12)$$

where the upper-script $B + \mu$ means that only the radiation from the muon leg was included (to compute it we used a modified leading-order version of the HECTOR program).

Then we applied to $d^2\sigma_{uncorr}/dx dy$ the full radiative correction factor (i.e. the third term in eq. (9)

$$\frac{d^2\sigma_{exp}^B(x_i^c, y_j^c, E_k^c)}{dxdy} = \frac{d^2\sigma_{uncorr}(x_i^c, y_j^c, E_k^c)}{dxdy} \frac{d^2\tilde{\sigma}^B(x_i^c, y_j^c, E_k^c)/dxdy}{d^2\tilde{\sigma}^{B+R}(x_i^c, y_j^c, E_k^c)/dxdy}. \quad (13)$$

In the original paper [6] Iron and Hydrogen data were normalised using $\sigma^{\nu Fe}/E_\nu = 0.625 \times 10^{-38} \text{cm}^2/\text{GeV}$ and $\sigma^{\bar{\nu} Fe}/E_{\bar{\nu}} = 0.3 \times 10^{-38} \text{cm}^2/\text{GeV}$. Since that time, the total νFe and $\bar{\nu} Fe$ cross sections have been measured more precisely [43]. We therefore applied a new overall correction factor corresponding to $\sigma^{\nu Fe}/E_\nu = 0.703 \times 10^{-38} \text{cm}^2/\text{GeV}$ and $\sigma^{\bar{\nu} Fe}/E_{\bar{\nu}} = 0.331 \times 10^{-38} \text{cm}^2/\text{GeV}$ [43]. We have also improved the overall normalisation of the Hydrogen data combining the CDHS [6] $\sigma^{\nu(\bar{\nu})H}/\sigma^{\nu(\bar{\nu})Fe}$ and BEBC [47] $\sigma^{\nu(\bar{\nu})H}/\sigma^{\nu(\bar{\nu})Ne}$ results. Assuming no correlations between these experiments, we determined the absolute normalisation of the CDHS Hydrogen data using: $\sigma^{\nu H}/E_\nu = 0.451 \times 10^{-38} \text{cm}^2/\text{GeV}$ and $\sigma^{\bar{\nu} H}/E_{\bar{\nu}} = 0.473 \times 10^{-38} \text{cm}^2/\text{GeV}$. The remaining error is 3.3% for the neutrino beam and 5.3% for the anti-neutrino beam. In summary, the νFe , $\bar{\nu} Fe$, νH and $\bar{\nu} H$ published CDHS data have been renormalised by +12.5%, +10.3%, +14.5% and +20.6% respectively.

3.1.3 BEBC measurements

Among the BEBC publications only one [5] gives enough information to reconstruct the differential cross sections without any QCD assumptions. In this article, the corrected number of events is given in bins of x and y for a given range of Q^2 . As in the case of the CDHS data, the radiative corrections were applied incompletely, considering only the radiation from the muon leg. Hence we uncorrected the published BEBC data analogously to what we did for CDHS (except that now we have *number of events* instead of *differential cross sections*)

$$N_{ijk}^{uncorr} = N_{ijk}^{publ} \cdot \frac{\int_{x_i}^{x_{i+1}} \int_{y_j}^{y_{j+1}} \int_{E_{min}}^{E_{max}} \frac{d\phi}{dE} \frac{d^2\tilde{\sigma}^{B+\mu}(x, y, E)}{dxdy} dx dy dE}{\int_{x_i}^{x_{i+1}} \int_{y_j}^{y_{j+1}} \int_{E_{min}}^{E_{max}} \frac{d\phi}{dE} \frac{d^2\tilde{\sigma}^B(x, y, E)}{dxdy} dx dy dE}. \quad (14)$$

Then we inserted N_{ijk}^{uncorr} into eq. (10) and constructed the ‘experimental’ Born cross section

$$\frac{d^2\sigma_{exp}^B(x_i^c, y_j^c, E_k^c)}{dxdy} = \frac{N_{ijk}^{uncorr}}{C} \cdot \frac{d\tilde{\sigma}^B(x_i^c, y_j^c, E_k^c)/dxdy}{\int_{x_i}^{x_{i+1}} \int_{y_j}^{y_{j+1}} \int_{E_{min}}^{E_{max}} \frac{d\phi}{dE} \frac{d^2\tilde{\sigma}^{B+R}(x, y, E)}{dxdy} dE dx dy}. \quad (15)$$

To compute the correction factors, the beam energy flux function of [48] was used⁶ and the kinematic cuts applied in the data analysis were taken into account:

⁶We thank U. Katz for having provided us the FORTRAN code computing the beam energy fluxes used in [48].

$Q^2 > 2\text{GeV}^2$, $W^2 > 4\text{GeV}^2$, $5 < E < 160$ GeV and $E_\mu > 5$ GeV (E_μ being the scattered muon energy).

One should notice that: *i*) The beam energy flux is not known absolutely, hence the absolute normalisation of the data has to be determined by the global fit. *ii*) The systematic errors are not available.

3.2 Nuclear effects

Most of the neutrino DIS data come from experiments with nuclear targets (deuteron or heavy nuclei). Thus they have to be corrected for nuclear effects, which are known to be quite relevant (see for instance [49, 50]).

3.2.1 Deuteron

We correct the calculated nucleon structure functions for nuclear binding, Fermi motion and off-shell effects using the results of the covariant approach of Melnitchouk et al. [51]⁷. The neutrino structure functions $F_1^{\nu D}$, $F_2^{\nu D}$ and $F_3^{\nu D}$ are treated analogously.

The calculation of [51] describes only the high- x ($x \gtrsim 0.2$) behaviour of the deuteron structure functions. At small x other mechanisms are at work (anti-shadowing and shadowing) but they are negligible in the x and Q^2 regions of the deuteron data entering our analysis [52].

3.2.2 Heavy nuclei

All CDHSW and a large fraction of CDHS data are obtained from scattering off Iron nuclei. Since the theoretical understanding of nuclear effects in heavy nuclei is still uncertain and model dependent [49, 50], we adopt an empirical procedure to perform the nuclear corrections.

The experimental $\nu(\bar{\nu})Fe$ differential cross sections are fitted to

$$d\sigma^{\nu(\bar{\nu})Fe} = \frac{d\sigma_{iso}^{\nu(\bar{\nu})Fe}}{R_{iso}^{\nu(\bar{\nu})}} , \quad (16)$$

where $R_{iso}^{\nu(\bar{\nu})}$ is the correction factor for the non-isoscalarity of Iron

$$R_{iso}^{\nu(\bar{\nu})} = \frac{(d\sigma^{\nu(\bar{\nu})p} + d\sigma^{\nu(\bar{\nu})n})/2}{(Z d\sigma^{\nu(\bar{\nu})p} + (A - Z) d\sigma^{\nu(\bar{\nu})n})/A} \quad (A = 55.8, Z = 26) , \quad (17)$$

and $d\sigma_{iso}^{\nu(\bar{\nu})Fe}$ is the ‘isoscalar’ Iron cross section which incorporates the nuclear corrections. Thus

$$d\sigma_{iso}^{\nu(\bar{\nu})Fe} = d\sigma^{\nu(\bar{\nu})D} \cdot R_{nucl}^{iso}$$

⁷We thank W. Melnitchouk for having provided us the computer code of his calculation.

where R_{nucl}^{iso} is a function embodying the nuclear effects on an isoscalar target. R_{nucl}^{iso} consists of two factors

$$R_{nucl}^{iso} = R_{Fe/D} \cdot R_{iso}^\ell. \quad (18)$$

The first factor is the Fe/D structure function ratio

$$R_{Fe/D} = \frac{F_2^{Fe}}{F_2^D}, \quad (19)$$

which is obtained from a fit to the published experimental data on F_2^{Fe}/F_2^D , uncorrected for isoscalarity. The second factor contains the isoscalarity corrections

$$R_{iso}^\ell = \frac{(F_2^{\ell p} + F_2^{\ell n})/2}{(Z F_2^{\ell p} + (A - Z) F_2^{\ell n})/A}. \quad (20)$$

$R_{Fe/D}$ is a function of x only because there is no experimental evidence of a significant Q^2 dependence (for a recent study, see [53]). Theoretically, a higher-twist (*i.e.* power-like) Q^2 dependence is expected at small x and $Q^2 \sim 1$ GeV 2 [54, 55], but at larger Q^2 , in the region covered by our analysis, shadowing is a scaling phenomenon [56, 57].

The small- x ($x < 0.1$) νFe and $\bar{\nu} Fe$ are excluded in our analysis. The reason is that in this region there are a number of uncertainty sources affecting the determination of R_{nucl} . First of all, there is an unsolved discrepancy between the two measurements $R_{Fe/D}$ at small- x , namely between E665 [58] and NMC [53]. Second, the use of the *charged-lepton* DIS data to determine the Fe/D ratio of *neutrino* cross sections in eq. (16) is justified by the BEBC *Ne* target results [59] being in good agreement with the NMC results on C [53] (see [1]), but the situation is experimentally not so clear for $x \lesssim 0.1$, where different nuclear corrections for charged lepton and neutrino structure functions are expected from a theoretical point of view [60]. Finally, the F_2 and $x F_3$ corrections might be different at small x [61]. Thus the cut at $x = 0.1$ removes from our fits the more controversial kinematic region as for nuclear corrections.

We have then performed a fit to the SLAC [62] BCDMS [63] $F_2^{\mu Fe}/F_2^{\mu D}$ data in the range $0.1 < x < 0.65$. For the function $R_{Fe/D}(x)$ we chose the empirical form

$$R_{Fe/D}(x) = \alpha_1 + \alpha_2 x + \alpha_3 x^2 \quad (21)$$

where α_i , $i = 1, 2, 3$ are the free parameters of the fit. The parameters $\bar{\alpha}_i$ minimising the χ^2 of this fit (we shall denote it $\chi^2_{Fe/D}$) are given in Table 4. The result of the fit is shown in fig. 3 together with the one-standard-deviation error band.

In fig. 4.a,b we plotted the isoscalarity and nuclear+isoscalarity corrections computed from the structure functions obtained with our fit (see section 5).

| $\bar{\alpha}_1$ | $\bar{\alpha}_2$ | $\bar{\alpha}_3$ |
|-------------------|------------------|------------------|
| 1.091 ± 0.021 | -0.34 ± 0.12 | -0.09 ± 0.16 |

Table 4: Results of the minimisation of $\chi^2_{Fe/D}$ (see text).

4 The analysis

4.1 Data entering the fit

Our analysis includes the neutrino and anti-neutrino cross section data of BEBC [5], CDHS [6] and CDHSW [7]. The number of collected events, the number of points and the kinematic domain covered by these experiments are listed in Table 5.

Besides the neutrino data, discussed at length in section 3, the bulk of data entering our fits consist of structure functions from various charged-lepton DIS experiments: BCDMS [11], H1 [12], NMC [10] (see Table 6).

As for BCDMS, we do not use the merged structure function data, obtained by putting together measurements at different beam energies, but rather the data on the reduced cross section

$$\frac{Q^2}{4\pi\alpha_{em}^2 M_N E} \frac{1}{Y} \frac{d^2\sigma}{dxdy}, \quad Y = 1 + (1 - y)^2 - \frac{M_N xy}{E}, \quad (22)$$

for each beam energy (we retrieved the original data from ref. [64]).

| | events | Δx | ΔQ^2 (GeV 2) | Δy |
|-------------------------|---------|----------------|--------------------------|----------------|
| CDHSW(νFe) | 640 000 | $0.015 - 0.65$ | $0.2 - 240$ | $0.037 - 0.87$ |
| CDHSW($\bar{\nu} Fe$) | 550 000 | " | " | " |
| CDHS(νH) | 2 100 | " | " | " |
| CDHS($\bar{\nu} H$) | 1 100 | " | " | " |
| BEBC(νD) | 12 100 | $0.03 - 0.65$ | $3 - 75$ | $0.05 - 0.95$ |
| BEBC($\bar{\nu} D$) | 5 400 | " | " | " |
| BEBC(νH) | 9 800 | $0.03 - 0.65$ | $3 - 75$ | $0.05 - 0.95$ |
| BEBC($\bar{\nu} H$) | 4 900 | " | " | " |

Table 5: Number of events and limits of the kinematic domain covered by the neutrino experiments considered in our analysis.

To avoid a redundancy of data sets and, most of all, to limit the number of experimental parameters in the χ^2 minimisation, the CDHS Iron data, which are in agreement with the CDHSW data, do not enter the fit. For the same reasons, the ZEUS F_2 data [65] are not included (ZEUS and H1 1994 data are consistent within 1 – 2%, as shown by a recent pQCD analysis [66]).

| | Δx | ΔQ^2 (GeV 2) |
|------------------------|----------------------------|--------------------------|
| NMC ($\mu p, \mu D$) | 0.008 – 0.5 | 0.8 – 60 |
| BCDMS (μp) | 0.07 – 0.75 | 7.5 – 230 |
| H1-94 (ep) | $3.2 \cdot 10^{-5} – 0.32$ | 1.5 – 5000 |
| E605 (DY) | 0.12 – 0.4 | 22.6 – 248 |
| NA51 (DY) | 0.18 | 27.2 |
| E866 (DY) | 0.036 – 0.312 | 30 – 164 |

Table 6: Kinematic range of the charged-lepton DIS and DY data sets entering our fits.

Drell-Yan (DY) data are introduced in order to constrain the non-strange sea. Three measurements are used. We fitted the differential cross section for the reaction $pCu \rightarrow \mu^+ \mu^- X$ measured by E605 [13]. The cross section is calculated at NLO⁸. For Drell-Yan processes the charm contribution is small [68] and is neglected in our analysis. No higher twist corrections are required [69] since the kinematic domain covered by E605 avoids the phase space boundaries where these corrections are expected to be important⁹.

The other Drell-Yan results that we use are the measurements of the DY asymmetry in pp and pD collisions by NA51 [14] and by E866 [15]. These data constrain the ratio \bar{u}/\bar{d} .

The kinematic cuts applied to the DIS data entering the fit are:

- $Q^2 \geq 3.5$ GeV 2 and $W^2 \geq 10$ GeV 2 .

In this region higher-twist effects are negligible [71]. Target mass corrections [72] are also very small but have been taken into account in our calculations.

Due to the W^2 and Q^2 cuts neither the E665 [73], nor the H1 (1995) [74], nor the SLAC [41], nor the ZEUS (1995) F_2 data [75] enter our fits.

Finally, we reject the CDHSW data with $x < 0.1$. The reason for this cut is threefold: *i*) the systematic errors in the low- x region are large [44]; *ii*) the nuclear corrections at small x are not completely under control, as discussed in section 3.2; *iii*) at low- x the CDHSW results disagree with the CCFR findings for the cross sections [76] and for the structure functions [3].

4.2 Fitting procedure

The main steps of our fitting procedure are summarised below. For each iteration:

⁸ We thank W. van Neerven for having provided us the code computing the order α_s Wilson coefficients published in [67].

⁹This is not the case for the latest E772 Drell-Yan data [70] and that is why we do not consider them here.

1. The pdf's are parametrised at a given value of the momentum transfer denoted Q_0 . We choose $Q_0^2 = 4 \text{ GeV}^2$.
2. The DGLAP equations are solved numerically in the x -space [77] (see [78] for a comparison of different NLO evolution codes).
3. The evolved pdf's are convoluted with the Wilson coefficients to obtain the structure functions (see section 2).
4. Assuming that all experimental uncertainties are normally distributed the χ^2 is computed

$$\begin{aligned}
\chi^2 &= \sum_{exp} \sum_{dat} \frac{[\mathcal{O}_{exp}^{dat} - \mathcal{O}^{fit} \times (1 - \nu_{exp} \sigma_{exp} - \sum_k \delta_k^{dat}(s_k^{exp}))]^2}{\sigma_{dat,stat}^2 + \sigma_{dat,uncor}^2} \\
&+ \sum_{exp} \nu_{exp}^2 + \sum_{exp} \sum_k (s_k^{exp})^2 \\
&+ \sum_{i,j=1}^2 [(a_i^\nu - \bar{a}_i^\nu) M_{ij}^\nu (a_j^\nu - \bar{a}_j^\nu) + (a_i^{\bar{\nu}} - \bar{a}_i^{\bar{\nu}}) M_{ij}^{\bar{\nu}} (a_j^{\bar{\nu}} - \bar{a}_j^{\bar{\nu}})], \quad (23)
\end{aligned}$$

where \mathcal{O} stands for the observables (structure functions and differential cross sections). The first two sums run over the data (*dat*) of the various experiments (*exp*); σ_{exp} is the relative overall normalisation uncertainty; $\sigma_{dat,stat}$ and $\sigma_{dat,uncor}$ are the statistical error and the uncorrelated systematic error, respectively, corresponding to the datum *dat*; ν_{exp} is the number of standard deviations corresponding to the overall normalisation of the experimental sample *exp*; $\delta_k^{dat}(s_k^{exp})$ is the relative shift of the datum *dat* induced by a change by s_k^{exp} standard deviations of the k^{th} correlated systematic uncertainty source of the experiment *exp*. It is estimated by

$$\begin{aligned}
\delta_k^{dat}(s_k^{exp}) &= \frac{\mathcal{O}_{exp}^{dat}(s_k^{exp} = +1) - \mathcal{O}_{exp}^{dat}(s_k^{exp} = -1)}{2\mathcal{O}_{exp}^{dat}} s_k^{exp} + \\
&\left[\frac{\mathcal{O}_{exp}^{dat}(s_k^{exp} = +1) + \mathcal{O}_{exp}^{dat}(s_k^{exp} = -1)}{2\mathcal{O}_{exp}^{dat}} - 1 \right] (s_k^{exp})^2
\end{aligned}$$

where $\mathcal{O}_{exp}^{dat}(s_k^{exp} = \pm 1)$ is the experimental determination of \mathcal{O}_{exp}^{dat} obtained varying by $\pm 1\sigma$ the k^{th} source of uncertainty. The last term in eq. (23) has already been discussed in section 3.1.1 (eq. (11)).

Notice that even though the parameters ν_{exp} , s_k^{exp} , a_i^ν and $a_i^{\bar{\nu}}$ are obtained from the global χ^2 minimisation, they do not enter in the counting of the degrees of freedom since they are determined by the counter-terms.

The correlated systematic uncertainties are taken into account whenever the information about them is available. This is the case for H1 [12], BCDMS

[64] and NMC [10]. For CDHS and BEBC no information is available and for E605 [13] the uncorrelated systematic uncertainties are dominating. The systematic uncertainties of this later experiment has then been added in quadrature and included in $\sigma_{dat,uncor}^2$ of eq. (23). As already pointed out in section 3.1.3, the systematic uncertainties of the BEBC data are not known. Since these data cover the same region as the CDHS data, for both data sets we have taken into account only the statistical uncertainties (this has a negligible effect on the χ^2 minimisation, since the statistical significance of these samples is rather small).

5. The MIGRAD algorithm of the MINUIT program [79] is used to minimise the χ^2 .

Given the importance of nuclear effects in the treatment of the neutrino data, in parallel to the main fit, we performed, as a check, another fit, in which the nuclear parameters α_i of eq. (21) are not constrained to the values $\bar{\alpha}_i$ obtained by the independent parametrisation of the Fe/D structure function ratio described in section 3.2.2, but are readjusted a posteriori. This is done by adding the counter-term

$$\sum_{i,j=1}^3 (\alpha_i - \bar{\alpha}_i) M_{ij}^{Fe/D} (\alpha_j - \bar{\alpha}_j) \quad (24)$$

to the χ^2 expression of the global pQCD analysis. In eq. (24) $M_{ij}^{Fe/D} = (1/2) \partial^2 \chi_{Fe/D}^2 / \partial \alpha_i \partial \alpha_j$. We found that the two fits give very similar results.

4.3 The parametrisation

Imposing the isospin symmetry leads to the following relations among the pdf's: $u^p = d^n \equiv u$, $d^p = u^n \equiv d$, $\bar{u}^p = \bar{d}^n \equiv \bar{u}$, $\bar{d}^p = \bar{u}^n \equiv \bar{u}$, $s^p = s^n \equiv s$, $\bar{s}^p = \bar{s}^n \equiv \bar{s}$.

In our main fit, that we call **fit1**, the pdf's $u_v \equiv u - \bar{u}$, $d_v \equiv d - \bar{d}$, \bar{u} , \bar{d} , s , \bar{s} and g (the gluon density) are parametrised at $Q_0^2 = 4$ GeV² as follows:

$$xu_v(x, Q_0^2) = A_{u_v} x^{B_{u_v}} (1 - x)^{C_{u_v}} (1 + D_{u_v} x^{E_{u_v}}), \quad (25)$$

$$xd_v(x, Q_0^2) = A_{d_v} x^{B_{d_v}} (1 - x)^{C_{d_v}} (1 + D_{d_v} x^{E_{d_v}}), \quad (26)$$

$$x(\bar{u} + \bar{d})(x, Q_0^2) = A_+ x^{B_+} (1 - x)^{C_+} (1 + D_+ x^{E_+}), \quad (27)$$

$$x(\bar{d} - \bar{u})(x, Q_0^2) = A_- x^{B_-} (1 - x)^{C_-} (1 + D_- x), \quad (28)$$

$$xs(x, Q_0^2) = x\bar{s}(x, Q_0^2) = A_s x^{B_s} (1 - x)^{C_s} (1 + D_s x^{E_s}), \quad (29)$$

$$xg(x, Q_0^2) = A_g x^{B_g} (1 - x)^{C_g} (1 + D_g x^{E_g}). \quad (30)$$

This parametrisation form is similar to that used in [80] (we refer to this article for a justification of this choice).

Generally it is also assumed $s = \bar{s}$. The data samples used in the existing global analyses [19, 20, 21] cannot resolve in fact s and \bar{s} independently. In our case, the information coming from neutrino and anti-neutrino differential cross sections allows testing the hypothesis $s = \bar{s}$. We thus performed another fit, called **fit2**, allowing for a charge asymmetry in the strange sea, $s \neq \bar{s}$.

Some of the parameters in eqs. (25–30) are determined by physical constraints. One normalisation factor, say A_g , is fixed by the momentum sum rule, $\int_0^1 (xg + x \sum_i (q_i + \bar{q}_i)) dx = 1$. The two normalisation parameters A_{u_v} and A_{d_v} are fixed by the number sum rules $\int_0^1 u_v dx = 2$ and $\int_0^1 d_v dx = 1$.

While the intermediate- x and large- x shape of the strange distribution is well constrained by the data entering the fit, the small- x behaviour is not. Thus we set $B_s = B_+$. We also set $B_{u_v} = B_{d_v} = B_-$, as suggested by Regge theory. It is to be mentioned that, from a statistical point of view, these constraints do not worsen the χ^2 and are also required in order to get an invertible second derivative χ^2 matrix.

5 Results

We present now the results of our fits. The strong coupling is fixed at the value $\alpha_s(M_Z^2) = 0.120$ which is close to the world average [81].

The contributions of the different data sample to the χ^2 are given in table 7. The total χ^2 per degree of freedom is excellent for both fits. The amount of systematic corrections for each datum, that is the value of the term $[\nu_{exp}\sigma_{exp} + \sum_k \delta_k^{dat}(s_k^{exp})]$ in eq. (23), is between -6% and +12% for all fits.

The parameters of eqs. (25–30) are listed in table 8 and the parton densities are shown in fig. 5, where they are compared to the results of the other global fits. The momentum fractions of the various partons are listed in table 9.

The parton distributions in fig. 5 are accompanied by the error bands computed as explained in Appendix II. These do not take into account the uncertainties related to the functional choice of the pdf's, nor those inherent to the treatment of the errors, which are assumed to be normally distributed. The meaning of the error bands of our pdf's is the following. Once a specific form for the pdf's is chosen and the constraints described in section 4.3 are imposed, the error bands correspond to an increase of the χ^2 by one unit. Thus their width is determined not only by the abundance and the precision of the data but also by the constraints on the pdf's. This explains why the error bands may be small even in kinematic regions where there are no data.

With respect to the other parametrisations, our gluon density turns out to be higher at intermediate x . This can be due to the fact that we do not use the prompt photon data, which tend to favour a larger glue at high x and a smaller one at intermediate x . These data are still quite controversial and some of them seem to be in disagreement with the QCD predictions (for a recent discussion see

| Experiments | # pts | χ^2 fit1 | χ^2 fit2 | # exp param |
|-------------------------------|-------|-------------------------|-------------------------|----------------|
| BCDMS(100) $\sigma^{\mu p}$ | 94 | 108.0 | 110.8 | 12 |
| BCDMS(120) $\sigma^{\mu p}$ | 99 | 81.6 | 81.0 | |
| BCDMS(200) $\sigma^{\mu p}$ | 79 | 92.7 | 90.7 | |
| BCDMS(280) $\sigma^{\mu p}$ | 76 | 89.7 | 87.6 | |
| BCDMS(120) $\sigma^{\mu D}$ | 99 | 96.9 | 93.1 | |
| BCDMS(200) $\sigma^{\mu D}$ | 79 | 93.5 | 88.8 | |
| BCDMS(280) $\sigma^{\mu D}$ | 76 | 64.6 | 63.7 | |
| BEBC $\sigma^{\nu p}$ | 68 | 65.2 | 67.6 | 0 |
| BEBC $\sigma^{\bar{\nu} p}$ | 49 | 76.4 | 76.5 | |
| BEBC $\sigma^{\nu D}$ | 70 | 65.3 | 65.4 | |
| BEBC $\sigma^{\bar{\nu} D}$ | 49 | 49.7 | 46.7 | |
| CDHS $\sigma^{\nu p}$ | 45 | 50.6 | 48.6 | 2 |
| CDHS $\sigma^{\bar{\nu} p}$ | 42 | 53.7 | 53.2 | |
| CDHSW $\sigma^{\nu Fe}$ | 494 | 264.9 | 250.4 | 5 |
| CDHSW $\sigma^{\bar{\nu} Fe}$ | 492 | 274.2 | 277.5 | |
| E605(DY) | 136 | 104.9 | 104.1 | 1 |
| E866 A_{DY} | 11 | 8.2 | 8.2 | 1 |
| H1(94-svx) F_2^{ep} | 24 | 26.7 | 26.7 | 7 |
| H1(94-nvx) F_2^{ep} | 156 | 180.6 | 180.3 | |
| NMC(90) $F_2^{\mu p}$ | 34 | 32.6 | 32.5 | 16 |
| NMC(120) $F_2^{\mu p}$ | 46 | 67.0 | 67.3 | |
| NMC(200) $F_2^{\mu p}$ | 61 | 99.4 | 99.3 | |
| NMC(280) $F_2^{\mu p}$ | 68 | 106.1 | 105.6 | |
| NMC(90) $F_2^{\mu D}$ | 34 | 24.0 | 23.8 | |
| NMC(120) $F_2^{\mu D}$ | 46 | 50.6 | 50.8 | |
| NMC(200) $F_2^{\mu D}$ | 61 | 62.6 | 62.7 | |
| NMC(280) $F_2^{\mu D}$ | 68 | 94.8 | 95.6 | |
| NA51 A_{DY} | 1 | 2.7 | 2.7 | 0 |
| Total χ^2 | 2657 | 2430.8 | 2405.0 | 44 |

Table 7: Contribution to the global χ^2 , and number of points, of the data samples entering the fits. The values of the individual χ^2 's do not include the normalisation and correlated systematic shifts. The last column indicates the number of experimental parameters: overall normalisation of the data sets and correlated systematics. The contributions of the experimental parameters to the χ^2 amount to 43.6 for **fit1** and 40.5 for **fit2**.

| | fit1 | fit2 |
|---------------|--------|--------|
| A_g | 7.72 | 7.3 |
| B_g | 0.089 | 0.081 |
| C_g | 21.26 | 20.11 |
| D_g | 12072 | 6990 |
| E_g | 4.17 | 4.0 |
| A_{u_v} | 1.43 | 2.05 |
| B_{u_v} | 0.49 | 0.55 |
| C_{u_v} | 3.60 | 3.75 |
| D_{u_v} | 4.47 | 3.59 |
| E_{u_v} | 0.81 | 0.97 |
| A_{d_v} | 1.02 | 1.40 |
| B_{d_v} | 0.49 | 0.55 |
| C_{d_v} | 6.03 | 6.63 |
| D_{d_v} | 23.06 | 32.63 |
| E_{d_v} | 1.76 | 2.07 |
| A_+ | 0.071 | 0.075 |
| B_+ | -0.245 | -0.240 |
| C_+ | 8.31 | 8.62 |
| D_+ | 11.29 | 13.30 |
| E_+ | 0.88 | 0.97 |
| A_- | 0.11 | 0.12 |
| B_- | 0.49 | 0.55 |
| C_- | 16.08 | 16.31 |
| D_- | -55.62 | -58.46 |
| E_- | 1 | 1 |
| A_s | 0.064 | 0.066 |
| B_s | -0.245 | -0.240 |
| C_s | 5.31 | 5.59 |
| D_s | 443 | 11354 |
| E_s | 8.26 | 12.04 |
| $A_{\bar{s}}$ | 0.64 | 0.066 |
| $B_{\bar{s}}$ | -0.245 | -0.240 |
| $C_{\bar{s}}$ | 5.31 | 5.44 |
| $D_{\bar{s}}$ | 443 | 339 |
| $E_{\bar{s}}$ | 8.26 | 7.39 |

Table 8: Values of the parameters of the pdf's at $Q_0^2 = 4 \text{ GeV}^2$.

| Q^2 | g | u_v | d_v | \bar{u} | \bar{d} | s | \bar{s} |
|-----------------|----------------|----------------|----------------|---------------|---------------|---------------|---------------|
| 5 GeV 2 | 42.9 \pm 0.4 | 27.9 \pm 0.3 | 11.2 \pm 0.2 | 3.0 \pm 0.1 | 3.9 \pm 0.1 | 2.1 \pm 0.2 | 2.1 \pm 0.2 |
| | 42.8 \pm 0.5 | 27.9 \pm 0.3 | 11.2 \pm 0.2 | 2.9 \pm 0.1 | 3.8 \pm 0.2 | 2.3 \pm 0.2 | 2.2 \pm 0.2 |
| 20 GeV 2 | 46.6 \pm 0.3 | 24.6 \pm 0.3 | 9.8 \pm 0.2 | 3.2 \pm 0.1 | 4.0 \pm 0.1 | 2.4 \pm 0.2 | 2.4 \pm 0.2 |
| | 46.5 \pm 0.4 | 24.7 \pm 0.2 | 9.9 \pm 0.2 | 3.1 \pm 0.1 | 3.9 \pm 0.1 | 2.6 \pm 0.2 | 2.4 \pm 0.2 |
| 100 GeV 2 | 49.4 \pm 0.3 | 22.1 \pm 0.3 | 8.8 \pm 0.2 | 3.3 \pm 0.1 | 4.0 \pm 0.1 | 2.6 \pm 0.2 | 2.6 \pm 0.2 |
| | 49.3 \pm 0.3 | 22.1 \pm 0.2 | 8.8 \pm 0.2 | 3.3 \pm 0.1 | 4.0 \pm 0.1 | 2.8 \pm 0.2 | 2.7 \pm 0.2 |

Table 9: Fraction of the total nucleon momentum carried by the partons for three values of Q^2 . The results of **fit1** (upper row) and **fit2** (lower row) are displayed. The errors are computed as explained in Appendix II.

[82]). Also their compatibility with the DIS data is still an unsettled issue. Our glue is determined by DIS measurements only and might be in slight disagreement with the prompt photon data at medium and high x . We will explore this problem in a future work where we will make use of an enlarged dataset.

We also find a slight discrepancy in the d_v distribution between our results and the other global fits. This is not surprising, since in our parametrisation we did not include the CDF data on the lepton asymmetry in W production at the Tevatron [83]. These data constrain the u/d ratio at $x = 0.05 - 0.1$, which is precisely the region where some difference can be seen between our $d_v(x)$ and the CTEQ and MRST distributions.

The structure function F_2 measured in different charged lepton DIS experiments is shown in figs. 6, 7 and 8 with the curves of **fit1**. Our fits for the Drell-Yan data are presented in figs. 9 and 10. An excellent overall agreement is observed. In fig. 10.b we plotted the ratio \bar{d}/\bar{u} at $Q^2 = 30\text{GeV}^2$, together with its error band. Notice that the fit, which is dominated by the E866 data, yields a \bar{d}/\bar{u} ratio which lies below the NA51 determination.

The reduced ν ($\bar{\nu}$) differential cross section

$$\frac{d^2\sigma^r}{dxdy} = \frac{2\pi(M_W^2 + Q^2)^2}{G_F^2 M_N M_W^4 E} \frac{1}{Y} \frac{d^2\sigma}{dxdy}, \text{ with } Y = 1 + (1 - y)^2 - \frac{M_N xy}{E}, \quad (31)$$

computed from **fit1** is compared to the data in fig. 11 (Hydrogen target), fig. 12 (Deuterium) and fig. 13 (Iron). The BEBC and CDHS Hydrogen and Deuterium data are well fitted down to small x . These data contribute to constrain the valence distributions, without being affected by nuclear effects. Fig. 13 also shows that the CDHS Iron data, though not entering the fit, are well described by it. As for the CDHSW rejected data ($x < 0.1$), discrepancies with the fit appear only in the first bin $x = 0.045$ of figs. 13.

Figs. 13, 8, 6 and 7 and the χ^2 results of table 7 show explicitly that the ν and $\bar{\nu}$ Iron data are compatible with the data on F_2 coming from NC charged-lepton DIS even in the region $0.045 < x < 0.2$. By contrast, in [3, 84] a sizeable discrepancy

is found between the CCFR F_2^ν and the NMC F_2^μ . From the analysis performed here, which is done – we recall – on neutrino *cross sections*, no disagreement emerges between charged-lepton and neutrino DIS measurements. We checked that including in our analysis the CCFR structure functions the fit worsens. We also found that the F_3 data are much better described than the F_2 data. We do not give any quantitative information about the χ^2 of this particular fit since we considered the statistical errors only (the use of the total systematic uncertainties is not recommended by the CCFR Collaboration). In conclusion, some incompatibility seems to exist between the CCFR *structure functions* and all other charged-lepton and neutrino DIS data. A conclusive word on this matter could come from the analysis of the CCFR *cross sections*, which are unavailable at the moment.

The longitudinal structure function F_L and the longitudinal to transverse cross section ratio R

$$F_L = F_2 - \left(1 + \frac{4M_N^2 x^2}{Q^2}\right) 2x F_1, \quad R = \frac{F_2}{2x F_1} \left(1 + \frac{4M_N^2 x^2}{Q^2}\right) - 1$$

computed using the pdf's of **fit1** (we remind that all our fits include target mass corrections) are compared to the NMC [10] and BCDMS [11] results in fig. 14.a, to the H1 measurement [85] in fig. 14.b and to the CDHSW measurement [7] in fig. 14.c. Again, one can see a good agreement between our fit and the experimental results.

The beam energy dependence of the CDHSW νFe and $\bar{\nu} Fe$ data, resulting from the global χ^2 minimisation, is shown in fig. 2. The deviation from the independent linear fit of section 3.1.1 is small for $\bar{\nu} Fe$ data and larger for νFe .

5.1 The strange sea density

Let us concentrate now on the strange sea density. Due to the lack of data able to constrain it, this distribution plays a lesser role in the existing global fits. Two of them (CTEQ [19] and MRST [20]), guided by the results of the CCFR determination of $s(x)$ [22], in particular by the CCFR value of the strange-to-non-strange momentum ratio $\kappa \equiv \langle x(s + \bar{s}) \rangle / \langle x(\bar{u} + \bar{d}) \rangle \simeq 0.5$, impose

$$s(x) + \bar{s}(x) = \frac{1}{2} [\bar{u}(x) + \bar{d}(x)]. \quad (32)$$

In the GRV analysis [21], instead, the strange distribution is set to zero at the input scale, and then radiatively generated.

The abundance of our neutrino and anti-neutrino data sets allows us to fit $s(x)$ with no extra constraints. The resulting s distribution of **fit1** is shown, with its error band, in fig. 5, where it is compared with the other fits. Notice that it turns out to be closer to MRST and CTEQ at large x , and to GRV at

low x , where it is however much less constrained. From table 9 one sees that in **fit1** $\kappa = 0.67$ at $Q^2 = 20$ GeV 2 .

In fig. 15 $s(x)$ is plotted at three different Q^2 values, together with the CCFR results [22]. The agreement is good, although we must recall that the CCFR extraction of the strange distribution from dimuon production in $\nu(\bar{\nu})Fe$ DIS has been criticised in many respects [18, 24, 35, 86].

Fig. 16 shows quantitatively how **fit1** is favoured with respect to another fit, that we call **fit1b**, in which the constraint (32) is imposed. The total χ^2 of **fit1b** is 2492.4, higher than the χ^2 of **fit1** by 62 units. In fig. 16 we plotted the mean value of the so-called *pull* distribution, as a function of x , for the CDHSW data:

$$\langle pull \rangle_{x_{dat}} = \frac{1}{N_{exp}(x_{dat})} \sum_{dat} \frac{\mathcal{O}_{exp}^{dat} - \mathcal{O}^{fit}\{1 - \nu_{exp}\sigma_{exp} - \sum_k \delta_k^{dat}(s_k^{exp})\}}{\sqrt{\sigma_{dat,stat}^2 + \sigma_{dat,uncor}^2}}, \quad (33)$$

where $N_{exp}(x_{dat})$ is the number of data at $x = x_{dat}$ for the experiment exp . In our case exp stands for CDHSW(νFe) or CDHSW($\bar{\nu} Fe$). One can see from figs. 16.a and 16.b that it is the $\bar{\nu}$ data which tend to favour **fit1** with respect to **fit1b**.

A very interesting question is whether the strange distribution is equal or not to the anti-strange one. The usual assumption $s(x) = \bar{s}(x)$ is not dictated in fact by first principles.

We thus looked for a possible charge asymmetry of the strange sea performing a fit, called **fit2**, in which we release the constraint $s = \bar{s}$. From table 5, one can see that the attempt of disentangling the s and \bar{s} distributions is justified by the abundance of anti-neutrino events in our data set.

The parametrisation (29) for $s = \bar{s}$ is replaced in **fit2** by two independent functions for s and \bar{s}

$$xs(x, Q_0^2) = A_s x^{B_s} (1 - x)^{C_s} (1 + D_s x^{E_s}), \quad (34)$$

$$x\bar{s}(x, Q_0^2) = A_{\bar{s}} x^{B_{\bar{s}}} (1 - x)^{C_{\bar{s}}} (1 + D_{\bar{s}} x^{E_{\bar{s}}}). \quad (35)$$

We set $A_s = A_{\bar{s}}$ and $B_s = B_{\bar{s}}$, and we fix one more parameter by imposing $\int_0^1 (s - \bar{s}) dx = 0$ (no net strangeness).

The main results of **fit2** are:

- The minimum χ^2 decreases by 25 units with respect to **fit1** (see table 7). Hence the choice $s \neq \bar{s}$ is slightly favoured.
- The strange distribution turns out to be harder than the anti-strange one. The difference $s - \bar{s}$ is shown in fig. 17.a with its error band. In fig. 17.b we plot the ratio s/\bar{s} at $Q^2 = 20$ GeV 2 .
- The momentum fractions of the **fit2** partons at different Q^2 values are listed in table 9. The momentum fraction $\langle xs \rangle$ is larger than $\langle x\bar{s} \rangle$. Notice also that **fit2** favours a higher value for the strange-to-non-strange momentum ratio κ , with respect to the fit with $s = \bar{s}$.

Let us comment now on a previous test of the strange sea asymmetry. In [22] the CCFR Collaboration found no evidence for $s \neq \bar{s}$. In their analysis the constraint $s(x) = [\bar{u}(x) + \bar{d}(x)] \times A(1-x)^C$ was imposed, which limits the flexibility of the fit. Moreover, the dimuon sample of CCFR does not cover the high- x region and consists only of 5000 neutrino events and 1000 anti-neutrino events. Our analysis does not have these limitations (our data sample is much more balanced between neutrino and anti-neutrino events and no extra constraints are set but those ensuring no net strangeness), and gives a more precise result on s/\bar{s} , as one can see from fig. 17.

In order to understand how the difference $s - \bar{s}$ is constrained by the data, let us consider the quantity

$$\Delta^{\nu-\bar{\nu}} \equiv \frac{4\pi x(M_W^2 + Q^2)^2}{G_F^2 M_W^4} \left[\frac{d^2\sigma^{\nu N}}{dxdQ^2} - \frac{d^2\sigma^{\bar{\nu} N}}{dxdQ^2} \right]. \quad (36)$$

The flavour content of $\Delta^{\nu-\bar{\nu}}$ is more evident in the parton model where it reads

$$\Delta^{\nu-\bar{\nu}} \propto xs(x) - x\bar{s}(x) + Y_- [xu_v(x) + xd_v(x)], \quad (37)$$

with $Y_- = 1 - (1 - y)^2$. The $\nu - \bar{\nu}$ cross section difference (36) is plotted as a function of Y_- , at fixed x and Q^2 , in fig. 18. Comparing **fit1** and **fit2**, one can see that their results deviate with increasing x (being very close to each other for $x \lesssim 0.3$). At high- x **fit1** undershoots the CDHSW values of Δ^ν for all Q^2 bins. Fig. 18 shows that the CDHSW data are more precise at high- y . Hence it is this region which drives the result on $s - \bar{s}$. Looking at fig. 16.c,d one sees also that it is the ν data which favour **fit2** with respect to **fit1**.

Since the nuclear corrections applied to the CDHSW data are sizable (see fig. 4.b), one may naturally ask to what extent our results are affected by the uncertainties on the evaluation of these corrections. The Fe/D ratio, as we have seen (see fig. 3 and the check described at the end of section 4.2), is well determined by the charged lepton data. Moreover, it factorises in the $\nu - \bar{\nu}$ difference. Hence this component of the nuclear correction is rather harmless. The isoscalarity corrections are instead different for neutrino and anti-neutrino observables and quite large. Looking at eqs. (17, 20) one sees that the isoscalarity ratio cannot exceed $A/(2Z) = 1.073$ for Iron. Fig. 4.a shows that the maximal value we obtained is not far from this upper bound. We checked that reducing the isoscalarity ratio the resulting $s - \bar{s}$ difference gets larger. Thus we conclude that our results on the strange sea asymmetry are not spoiled, at least qualitatively, by the uncertainties on the isoscalarity corrections.

Theoretically, a charge asymmetric sea is accounted for by introducing a distinction between extrinsic and intrinsic $q\bar{q}$ pairs [87]. The extrinsic sea consists of short-lived quarks and anti-quarks produced by QCD hard subprocesses (bremsstrahlung and gluon splitting). It is evident that the extrinsic component of the sea cannot be charge asymmetric. On the other hand, the intrinsic $q\bar{q}$ pairs

exist over a longer time scale and are associated with nonperturbative phenomena. These pairs are still produced by gluon fragmentation but have time, before recombining, to interact with other partons. They represent higher Fock states of the nucleon ($|qqqq\bar{q}\dots\rangle$) and manifest themselves in meson–baryon fluctuations.

There is no fundamental principle forbidding a possible charge asymmetry of the intrinsic sea. Actually, there are reasons to believe that such asymmetry should indeed be a property of the strange and charmed sea [87, 88]. If the strange (or charmed) sea is asymmetric at low Q^2 due to some nonperturbative mechanism, the QCD evolution simply preserves this asymmetry because $s - \bar{s}$ (or $c - \bar{c}$) evolves like a non-singlet distribution and its first moment is constant. An interesting feature of the intrinsic sea is that it tends to exist at relatively large values of x [87, 88], corresponding to the most energetically favoured configuration of the nucleon light-cone wave function.

In the simplest model [89, 88] the production of the intrinsic strange sea is attributed to the $p \rightarrow \Lambda K^+$ fluctuation. Due to chiral symmetry pseudoscalar mesons have relatively small masses. As a consequence [88], the average x of the \bar{s} anti-quark in the K is smaller than the average x of the s quark coming from the Λ . Thus the s distribution is expected, on quite general grounds, to be harder than the \bar{s} distribution. This expectation has been substantiated by explicit calculations in [89, 90] (for other models see [91]). Our results on the strange and anti-strange sea density are, at least qualitatively, in agreement with the predictions of the intrinsic sea theory.

6 Conclusions

We have presented a global next-to-leading order QCD analysis of a large set of DIS data, including the (properly re-evaluated) neutrino and anti-neutrino differential cross sections of BEBC, CDHS, CDHSW, the charged-lepton structure functions of NMC, BCDMS and H1, and the Drell-Yan data of E605, NA51 and E866. The full use of the information on the nucleon structure embodied in neutrino DIS observables and a proper treatment of the experimental systematic uncertainties are the main novelties of our approach. In particular, the large-statistics CDHSW Iron data allow disentangling the strange sector from the non strange one: this leads to a consistent determination of $s(x)$ within a global fit, similarly to what happens for the other parton distributions.

The charm mass effects, whose relevance for an accurate determination of the parton densities is a recent firm acquisition, have been consistently treated in a massive factorisation scheme, the Fixed Flavour Scheme.

We found no evidence of any discrepancy between the neutrino data we considered in our fit and the charged-lepton data. A complete and unambiguous analysis of *all* neutrino experiments and a conclusive check of the compatibility of their data with the charged-lepton data would be possible only if we could use

the CCFR differential cross sections, which are unfortunately not available.

The large statistics of anti-neutrino events in our data sample allowed us to test the hypothesis of a charge asymmetric strange sea: $s \neq \bar{s}$. We found some evidence for such an asymmetry. The qualitative features of the resulting s and \bar{s} distributions (namely, a large x tail at low Q^2 and $\bar{s}(x)$ softer than $s(x)$) agree with the expectations of the intrinsic sea theory.

Finally, we outline some developments. As for the strong coupling, in the present work we took a pragmatic attitude, using the world average value. A more systematic study, in which we will extract α_s from the DIS data and investigate its correlation with the gluon density, will be presented in a forthcoming paper.

Another important development that we have in mind is the comparison of the results obtained in the two QCD massive schemes, FFS and VFS.

Finally, one should envisage some independent, and perhaps more direct, experimental test of the charge asymmetry of the strange sea for which we presented here only an indirect statistical evidence.

Acknowledgments

We thank J. Blümlein, V. Del Duca, S. Forte, G. Korchemski, M.W. Krasny, B.-Q. Ma, V. Massoud, W. Melnitchouk, A. Milsztajn, N.N. Nikolaev and W. Seligman for valuable help and/or useful discussions. Two of us (C.P. and F.Z.) would like to thank their H1 colleagues for their help in elaborating the pQCD analysis program.

Appendix I: Unfolding procedure

A two dimension net in x and y is defined. The nodes correspond to the centres of the experimental bins. Following [77], we define a basis of continuous functions $\phi_i(x)$ and $\psi_j(y)$ such that $\phi_i(x_l^c) = \delta_{il}$ and $\psi_j(y_m^c) = \delta_{jm}$ (where δ_{il} is the Kronecker symbol). Provided these functions are determined using a spline interpolation [92], the differential cross section can be written as

$$\frac{d^2\sigma^{\nu(\bar{\nu})Fe}(x, y, E_k^c)}{dxdy} = \sum_{l=1}^{n_x} \sum_{m=1}^{n_y} \phi_i(x) \psi_j(y) \frac{d^2\sigma^{\nu(\bar{\nu})Fe}(x_l^c, y_m^c, E_k^c)}{dxdy}. \quad (38)$$

Applying the average theorem, eq. (38) leads to

$$\sigma_{ijk} = \sum_{l=1}^{n_x} \sum_{m=1}^{n_y} c_x^{i,l} c_y^{j,m} \frac{d^2\sigma^{\nu(\bar{\nu})Fe}(x_l^c, y_m^c, E_k^c)}{dxdy} \quad (39)$$

with

$$\sigma_{ijk} \approx \frac{N_{ijk}}{C}, \quad c_x^{i,l} = \frac{\int_{x_i}^{x_{i+1}} \phi_l(x) dx}{x_{i+1} - x_i}, \quad c_y^{j,m} = \frac{\int_{y_j}^{y_{j+1}} \psi_m(y) dy}{y_{j+1} - y_j}$$

where N_{ijk} is the number of events experimentally observed and C is the number of scattering centres in the target.

The differential cross sections at the bin centres $d^2\sigma^{\nu(\bar{\nu})Fe}(x_l^c, y_m^c, E_k^c)/dxdy$ are obtained by reversing this system of $n_x \times n_y$ equations. Numerically, the more stable results were obtained using the first order spline. In this case, $\phi_i(x)$ and $\psi_j(y)$ are the Lagrange (or ‘hat’) functions [92]

$$\phi_i(x) = \begin{cases} (x - x_{i-1})/(x_i - x_{i-1}) & , x_{i-1} \leq x \leq x_i \\ (x_{i+1} - x)/(x_{i+1} - x_i) & , x_i \leq x \leq x_{i+1} \\ 0 & , \text{otherwise.} \end{cases} \quad (40)$$

The same expression holds for $\psi_j(y)$.

However, using eq. (40), one can see that the system of eq. (39) is incomplete if $x_1 \neq 0$ or $x_{n_x} \neq 1$ or $y_1 \neq 0$ or $y_{n_y} \neq 1$. Indeed, the boundary bins receive some contributions (in the r.h.s. of eq. (39)) coming from the bin neighbours which are not included in the measurements. To overcome this difficulty, we have defined artificial extra bins $[x_{n_x}, x_{n_x+1}] \forall y$, $[y_0, y_1] \forall x$ and $[y_{n_y}, y_{n_y+1}] \forall x$. Then we fixed the cross section at the centre of these new bins to a certain fraction λ of the closest cross section measurement. Under this modification, eq. (39) becomes an inhomogeneous system

$$\begin{aligned} \sigma_{i,j,k} - \lambda \left(c_x^{i,n_x+1} c_y^{j,0} \sigma_{n_x,1,k} + c_x^{i,n_x+1} c_y^{j,n_y+1} \sigma_{n_x,n_y,k} + \right. \\ \left. \sum_{m=1}^{n_y} c_x^{i,n_x+1} c_y^{j,m} \sigma_{n_x,j,k} + \sum_{l=1}^{n_x} c_x^{i,l} [c_y^{j,0} \sigma_{l,1,k} + c_y^{j,n_y+1} \sigma_{l,n_y,k}] \right) = \\ \sum_{l=1}^{n_x} \sum_{m=1}^{n_y} c_x^{i,l} c_y^{j,m} \frac{d^2\sigma^{\nu(\bar{\nu})Fe}(x_l^c, y_m^c, E_k^c)}{dxdy} \end{aligned} \quad (41)$$

and the differential cross sections at the bin centres are obtained by inverting this system with $\lambda = 1$.

In order to test the sensitivity of our results to the choice of λ , we have set λ to some extreme values: $\lambda = 2$, $\lambda = 1/2$. We observed a variation of the order of $\approx 20\%$ in the highest x bin for all y bins. But we point out that the results are completely stable in the first $x < 0.1$ bins for all y bins. This method is then used to perform the definitive bin centre correction in these particular bins, as mentioned in section 3.1.1. The uncertainty of the method is estimated by repeating the procedure using a second order spline interpolation to define the basis functions $\phi_i(x)$ and $\psi_j(y)$. The ratio of the two bin centre correction factors is then taken, bin by bin, as an estimate of the uncertainty due to the method, and added in quadrature to the uncorrelated systematic error of the measurement (it is of the order of $\lesssim 2\%$ and reaches 7.5% at high y).

Appendix II: Error bands

We describe here the formula used to calculate the error bands shown throughout the paper. Calling $\mathbf{p} \equiv \{p_1, \dots, p_n\}$ the vector of the free parameters of the fit, the error band of a given function f is given at each (x, Q^2) point by [93]:

$$\Delta f(x, Q^2; \mathbf{p}_0) = |f(x, Q^2; \mathbf{p}_0 + \Delta_p(x, Q^2)) - f(x, Q^2; \mathbf{p}_0 - \Delta_p(x, Q^2))| \quad (42)$$

where \mathbf{p}_0 denotes the parameter set minimising the χ^2 and the vector $\Delta_p(x, Q^2) \equiv \{\Delta_{p1}(x, Q^2), \dots, \Delta_{pn}(x, Q^2)\}$ is given by

$$\Delta_p(x, Q^2) = \frac{M^{-1} \partial_p f(x, Q^2; \mathbf{p})}{\sqrt{\partial_p f(x, Q^2; \mathbf{p}) M^{-1} \partial_p f(x, Q^2; \mathbf{p})}} \quad (43)$$

with $M_{ij} = (1/2) \partial^2 \chi^2 / \partial p_i \partial p_j$ and $\partial_p = \{\partial / \partial p_1, \dots, \partial / \partial p_n\}$.

References

- [1] See for instance:
 M. Diemoz, F. Ferroni and E. Longo, Phys. Rep. 130 (1986) 293.
 T. Sloan, G. Smadja and R. Voss, Phys. Rep. 162 (1988) 45.
 J.M. Conrad, M.H. Shaevitz and T. Bolton, Rev. Mod. Phys. 70 (1998) 1341.
 A.M. Cooper-Sarkar, R.C. Devenish, A. De Roeck, Int. J. Mod. Phys. A13 (1998) 3385.
- [2] See for instance, J.F. Owens and W.K. Tung, Annu. Rev. Nucl. Part. Sci. 42 (1992) 291.
- [3] W.G. Seligman, Ph.D. Thesis, Columbia University, Nevis Report-292 (1997).
- [4] W.K. Krasny, Habilitation Thesis, I.N.P Cracow, TPJU-22/89 (1989).
- [5] G.T. Jones et al., Z. Phys. C62 (1994) 575 and references therein.
- [6] H. Abramowicz et al., CDHS Collaboration, Z. Phys. C25 (1984) 29.
- [7] P. Berge et al., CDHSW Collaboration, Z. Phys. C49 (1991) 187.
- [8] F. Bergsma et al., CHARM Collaboration, Phys. Lett. B123 (1983) 269.
- [9] W.C. Leung et al., CCFR Collaboration, Phys. Lett. B317 (1993) 655; P.Z. Quintas et al., CCFR Collaboration, Phys. Rev. Lett. 71 (1993) 1307.
- [10] M. Arneodo et al., NMC Collaboration, Nucl. Phys. B483 (1997) 3.

- [11] A.C. Benvenuti et al., BCDMS Collaboration, *Phys. Lett.* B223 (1989) 485; *Phys. Lett.* B237 (1989) 592.
- [12] H1 Collaboration, *Nucl. Phys.* B470 (1996) 3.
- [13] G. Moreno et al., E605 Collaboration, *Phys. Rev.* D43 (1991) 2815.
- [14] A. Baldit et al., NA51 Collaboration, *Phys. Lett.* B332 (1994) 244.
- [15] E.A. Hawker et al., E866 Collaboration, *Phys. Rev. Lett.* 80 (1998) 3715.
- [16] A. Milsztajn et al., *Z. Phys.* C49 (1991) 527.
- [17] M. Gluck, E. Reya and M. Stratmann, *Nucl. Phys.* B422 (1994) 37.
- [18] V. Barone et al., *Phys. Lett.* B328 (1991) 143; *Phys. Lett.* B317 (1993) 433; *Z. Phys.* C70 (1996) 83.
- [19] H.L. Lai et al., CTEQ Collaboration, *Phys. Rev.* D55 (1997) 1280.
- [20] A.D. Martin, R.G. Roberts, W.J. Stirling and R.S. Thorne, *Eur. Phys. J.* C4 (1998) 463.
- [21] M. Glück, E. Reya and A. Vogt, *Eur. Phys. J.* C5 (1998) 461.
- [22] A.O. Bazarko et al., CCFR Collaboration, *Z. Phys.* C65 (1995) 189; A.O. Bazarko, Ph.D. Thesis, Columbia University, Nevis report 285.
- [23] M.A.G. Aivazis et al., *Phys. Rev.* D50 (1994) 3102.
- [24] V. Barone and M. Genovese, *Phys. Lett.* B379 (1996) 233.
- [25] V. Barone, U. D'Alesio and M. Genovese, in Proc. of the Workshop on Future Physics at HERA, G. Ingelman, A. De Roeck and R. Klanner eds., DESY (1996), p. 102.
- [26] W.J. Marciano, *Phys. Rev.* D29 (1984) 580.
- [27] E. Witten, *Nucl. Phys.* B104 (1976) 445. M. Glück and E. Reya, *Phys. Lett.* B83 (1979) 98.
- [28] W. Furmanski and R. Petronzio, *Z. Phys.* C11 (1982) 293.
- [29] W.L. van Neerven and E.B. Zijlstra, *Phys. Lett.* B272 (1991) 127; *Phys. Lett.* B273 (1991) 476; *Nucl. Phys.* B383 (1992) 525.
- [30] V.N. Gribov and L.N. Lipatov, *Sov. J. Nucl. Phys.* 15 (1972) 438; G. Altarelli and G. Parisi, *Nucl. Phys.* B126 (1977) 298; Yu.L. Dokshitzer, *Sov. Phys. JETP* 46 (1977) 641.

- [31] E. Laenen et al., Nucl. Phys. B392 (1993) 162, 229; Phys. Lett. B291 (1992) 325.
- [32] S. Riemersma, J. Smith and W.L. van Neerven, Phys. Lett. B347 (1995) 143.
- [33] T. Gottschalk, Phys. Rev. D23 (1981) 56.
- [34] U. D'Alesio, Ph.D. Thesis, Torino University (1996).
- [35] M. Glück, S. Kretzer and E. Reya, Phys. Lett. B380 (1996) 171; (E) ibid. B405 (1997) 391.
- [36] A. De Rùjula and R. Petronzio, Nucl. Phys. B154 (1979) 394.
- [37] D.Y. Bardin and O.M. Fedorenko, Yad. Phys. 30 (1979) 811.
- [38] D.Y. Bardin and V.A. Dokuchaeva, preprint JINR-E2-86-260 (1986).
- [39] J. Blümlein, Z. Phys. C65 (1995) 293.
- [40] A. Arbuzov et al., HECTOR program version 1.00, DESY 95-185.
- [41] L.W. Whitlow et al., Phys. Lett. B282 (1992) 475; L.W. Whitlow, Ph.D. Thesis, SLAC-Report-357 (1990).
- [42] A.J. Buras and K.J.F. Gaemers, Nucl. Phys. B132 (1978) 249.
- [43] P. Berge et al., CDHSW Collaboration, Z. Phys. C35 (1987) 443.
- [44] B. Vallage, Ph.D. Thesis, Université Paris 11 (1986), in French.
- [45] S.A. Rabinowitz et al., CCFR Collaboration, Phys. Rev. Lett. 70 (1993) 134.
- [46] P.H. Slander et al., CCFR Collaboration, Phys. Rev. D42 (1990) 759.
- [47] M. Aderholz et al., WA21 Collaboration, Phys. Lett. B173 (1986) 211.
- [48] U.F. Katz, Ph.D. Thesis, Max-Planck-Institut für Physik, München, MPI-PhE/92-03 (1992), in German.
- [49] V. Barone and E. Predazzi, Ann. Phys. Fr. 12 (1987) 525.
D.F. Geesaman, K. Saito and A.W. Thomas et al., Annu. Rev. Nucl. Part. Sci. 45 (1995) 337.
- [50] M. Arneodo, Phys. Rep. 240 (1994) 301.
- [51] W. Melnitchouk, A.W. Schreiber and A.W. Thomas, Phys. Lett. B335 (1994) 11.

- [52] V. Barone et al., *Phys. Lett.* B321 (1994) 137.
B. Badełek and J. Kwieciński, *Phys. Rev.* D50 (1994) 4.
- [53] A. Amaudruz, NMC Collaboration, *Nucl. Phys.* B441 (1995) 3; M. Arneodo et al., NMC Collaboration *Nucl. Phys.* B441 (1995) 12.
- [54] J. Kwieciński and B. Badełek, *Phys. Lett.* B208 (1988) 508.
- [55] W. Melnitchouk and A.W. Thomas, *Phys. Rev.* C52 (1995) 3373.
- [56] N.N. Nikolaev and V.I. Zakharov, *Phys. Lett.* 55B (1975) 397;
N.N. Nikolaev and B.G. Zakharov, *Z. Phys.* C49 (1991) 607.
- [57] V. Barone et al., *Z. Phys.* C58 (1993) 541.
- [58] M.R. Adams et al., E665 Collaboration, *Z. Phys.* C67 (1995) 403.
- [59] P.P. Allport et al., WA59 Collaboration, *Phys. Lett.* B232 (1989) 417.
- [60] B.Z. Kopeliovich and P. Marage, *Int. J. Mod. Phys.* A8 (1993) 1513.
- [61] R. Kobayashi, S. Kumano and M. Miyama, *Phys. Lett.* B354 (1995) 465.
- [62] J. Gomez et al., E139 Collaboration, *Phys. Rev.* D49 (1994) 4348.
- [63] A.C. Benvenuti et al., BCDMS Collaboration, *Phys. Lett.* B189 (1987) 483.
- [64] A.C. Benvenuti et al., BCDMS Collaboration, CERN-EP/89-06; CERN-EP/89-170.
- [65] M. Derrick et al., ZEUS Collaboration, *Z. Phys.* C72 (1996) 399.
- [66] F. Lehner, Ph.D. Thesis, University of Hamburg (1998), in German.
- [67] P.J. Rijken and W.L. van Neerven, *Phys. Rev.* D51 (1995) 44.
- [68] P.J. Rijken and W.L. van Neerven, *Phys. Rev.* D52 (1995) 149.
- [69] M. Dasgupta and B.R. Webber, *Phys. Lett.* B382 (1996) 273; Y.L. Dokshitzer et al., *Nucl. Phys.* B469 (1996) 93.
- [70] P.L. McGaughey et al., E772 Collaboration, *Phys. Rev.* D50 (1994) 3038.
- [71] M. Virchaux and A. Milsztajn, *Phys. Lett.* B274 (1992) 221.
- [72] H. Georgi and H.D. Politzer, *Phys. Rev.* D14 (1976) 1829. R. Barbieri et al., *Nucl. Phys.* B117 (1976) 50.
- [73] M.R. Adams et al., E665 Collaboration, *Phys. Rev.* D54 (1996) 3006.

- [74] C. Adloff et al., H1 Collaboration, Nucl. Phys. B497 (1997) 3.
- [75] J. Breitweg et al., ZEUS Collaboration, Phys. Lett. B407 (1997) 432.
- [76] U.K. Yang et al., CCFR Collaboration, J. Phys. G22 (1996) 775.
- [77] C. Pascaud and F. Zomer, DESY preprint DESY/96-266.
- [78] J. Blümlein et al., in Proc. of the Workshop on Future Physics at HERA, G. Ingelman, A. De Roeck and R. Klanner eds., DESY (1996), p. 23.
- [79] CERN Program Library Long Writeup D506, CERN (1993).
- [80] H.L. Lai et al., CTEQ Collaboration, Phys. Rev. D51 (1995) 4763.
- [81] Particle Data Group, Review of Particle Properties, Eur. Phys. J. C3 (1998) 1.
- [82] P. Aurenche et al., Eur. Phys. J. C9 (1999) 107.
- [83] F. Abe et al., CDF Collaboration, Phys. Rev. Lett. 74 (1995) 850.
- [84] W.G. Seligman et al., CCFR Collaboration, Phys. Rev. Lett. 79 (1997) 1213.
- [85] C. Adloff et al., H1 Collaboration, Phys. Lett. B393 (1997) 452.
- [86] M. Glück, S. Kretzer and E. Reya, Phys. Lett. B398 (1997) 381; (E) ibid. B405 (1997) 392.
- [87] S.J. Brodsky, P. Hoyer, C. Peterson and N. Sakai, Phys. Lett. B93 (1980) 451; S.J. Brodsky, C. Peterson and N. Sakai, Phys. Rev. D23 (1981) 2745.
- [88] M. Burkardt and B.J. Warr, Phys. Rev. D45 (1992) 958.
- [89] A.I. Signal and A.W. Thomas, Phys. Lett. B191 (1987) 205.
- [90] S.J. Brodsky and B.-Q. Ma, Phys. Lett. B381 (1996) 317.
H. Holtmann, A. Szczurek and J. Speth, Nucl. Phys. A596 (1996) 631;
A. Szczurek, A.J. Buchmann and A. Faessler, J. Phys. G22 (1996) 1741.
- [91] X. Ji and J. Tang, Phys. Lett. B362 (1995) 182.
W. Melnitchouk and M. Malheiro, hep-ph/9901321.
- [92] C. de Boor, *A practical guide to spline*, Springer-Verlag (1978).
- [93] C. Pascaud and F. Zomer, LAL preprint LAL/95-05.

$E = 111 \text{ GeV}$

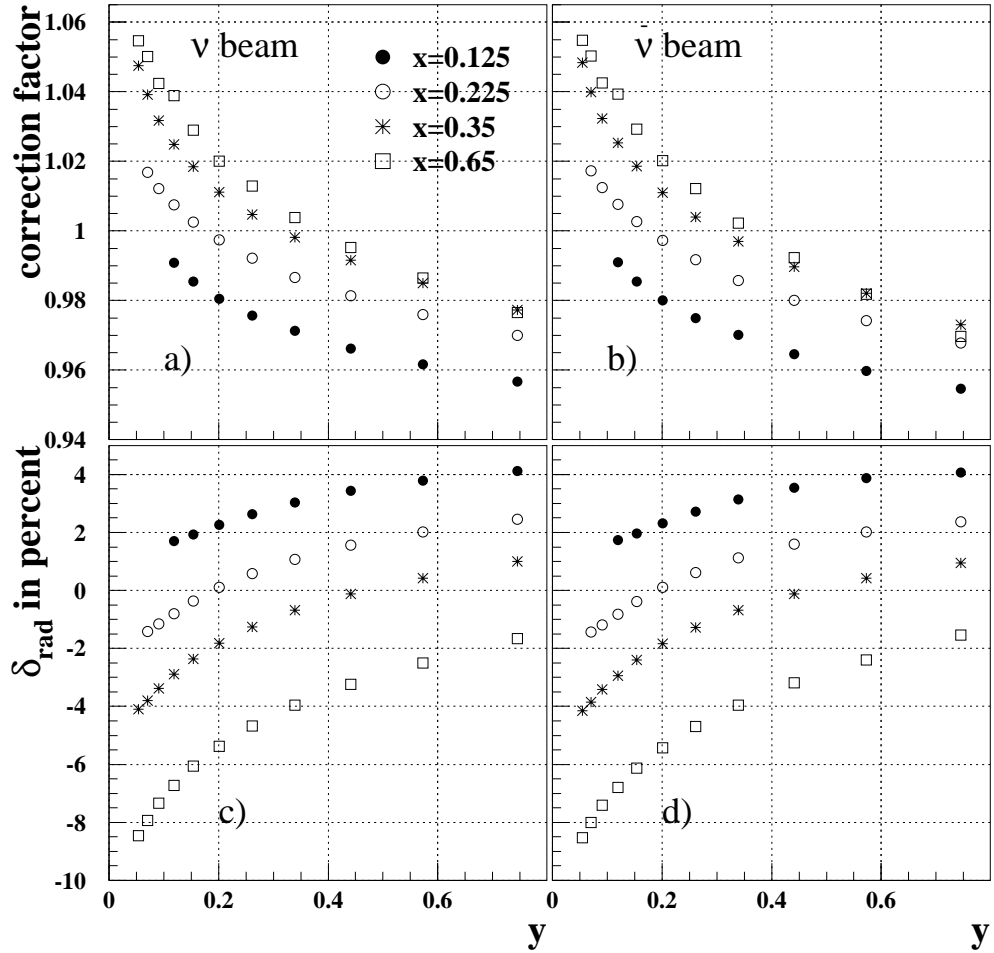


Figure 1: a) Correction factor applied to CDHSW νFe data of the 111 GeV beam energy sample, as a function of y for various x bins; b) same as a) but for CDHSW $\bar{\nu} Fe$ data; c) electroweak radiative correction factor $\delta_{rad} \equiv (d^2\tilde{\sigma}^{B+R}/dxdy)/(d^2\tilde{\sigma}^B/dxdy) - 1$ in percent for CDHSW νFe ; d) same as c) but for CDHSW $\bar{\nu} Fe$.

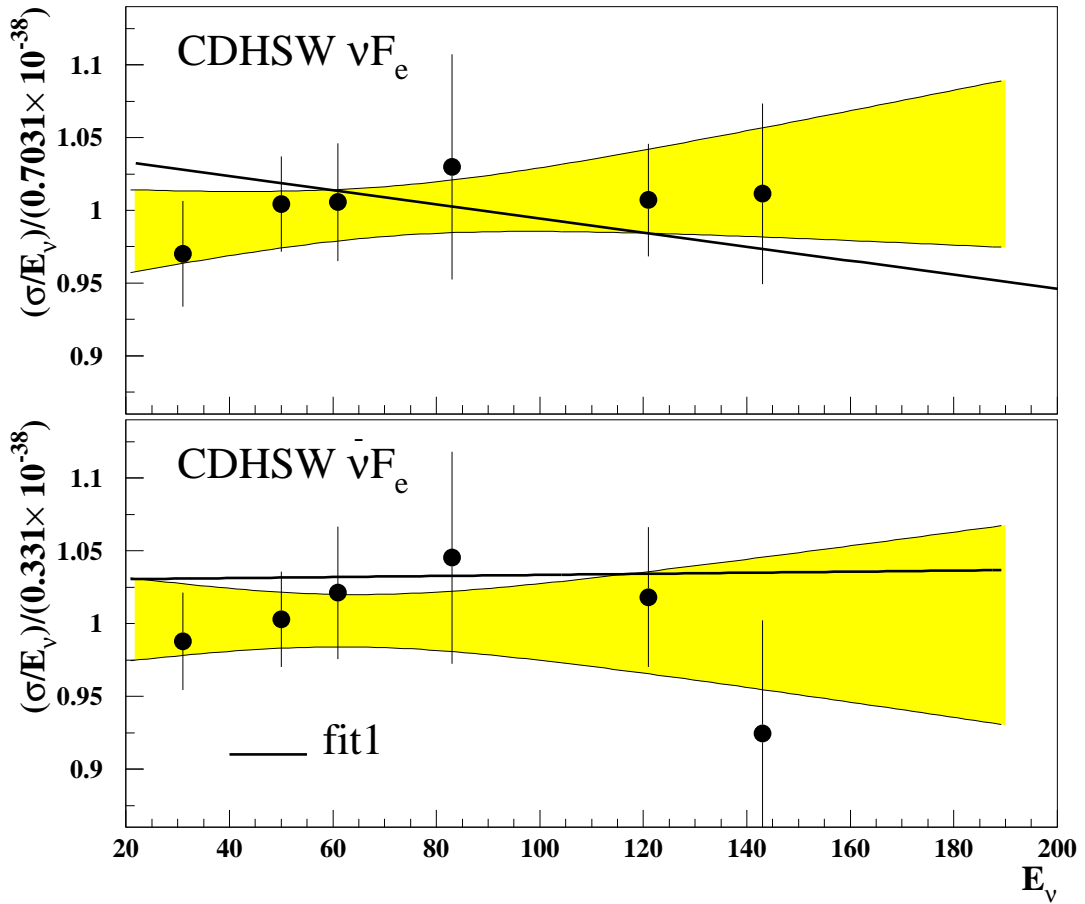


Figure 2: Total cross sections of νFe (top) and $\bar{\nu} Fe$ (bottom) from CDHSW. The shaded areas are the one-standard-deviation error bands corresponding to the linear fits described in section 3.1.1. The curves are the results of **fit1**. The error bars correspond to the quadratic sum of statistical and systematic errors.

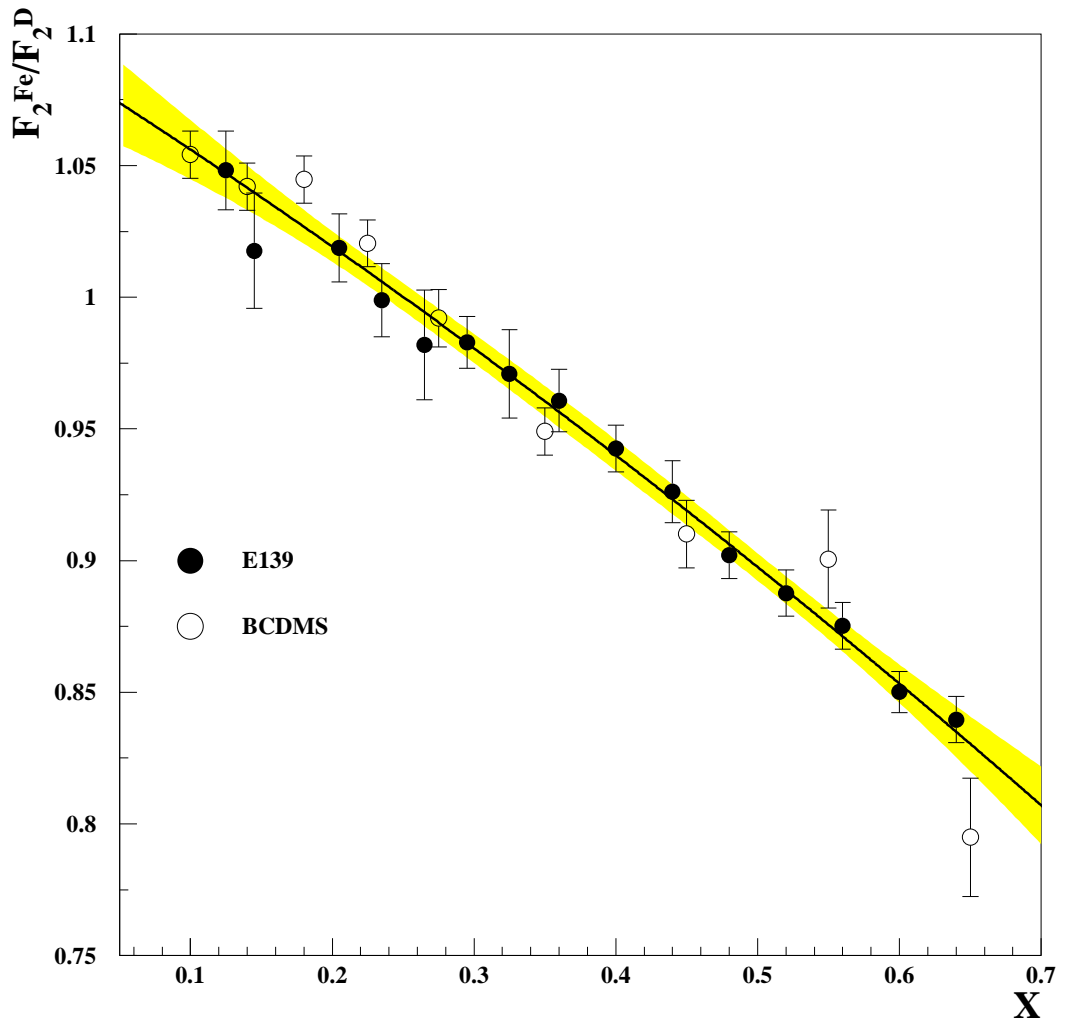


Figure 3: Fe/D structure function ratio. The full line is the result of a second order polynomial fit and the shaded area is the corresponding one-standard-deviation error band (see section 3.2). The error bars correspond to the quadratic sum of statistical and systematic errors.

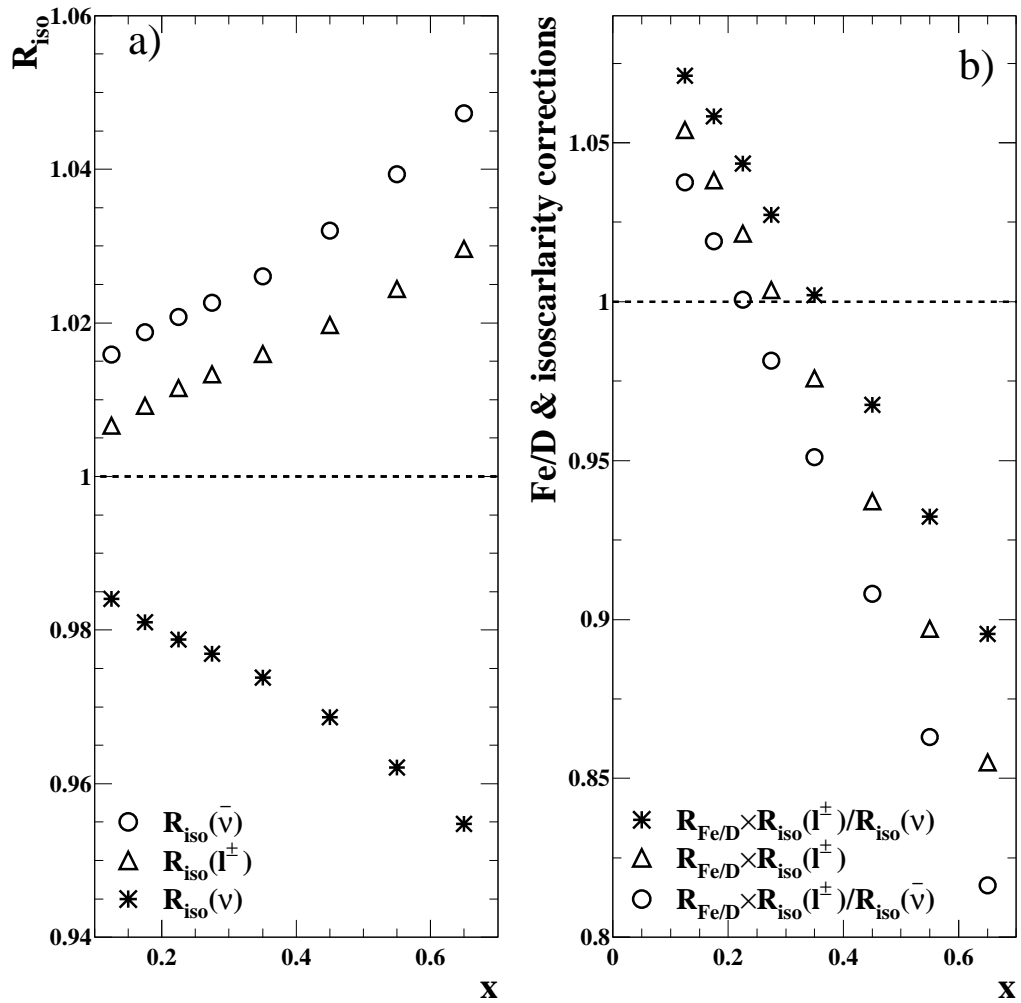


Figure 4: Corrections applied to Iron target data: a) isoscalarity corrections; b) nuclear and isoscalarity corrections.

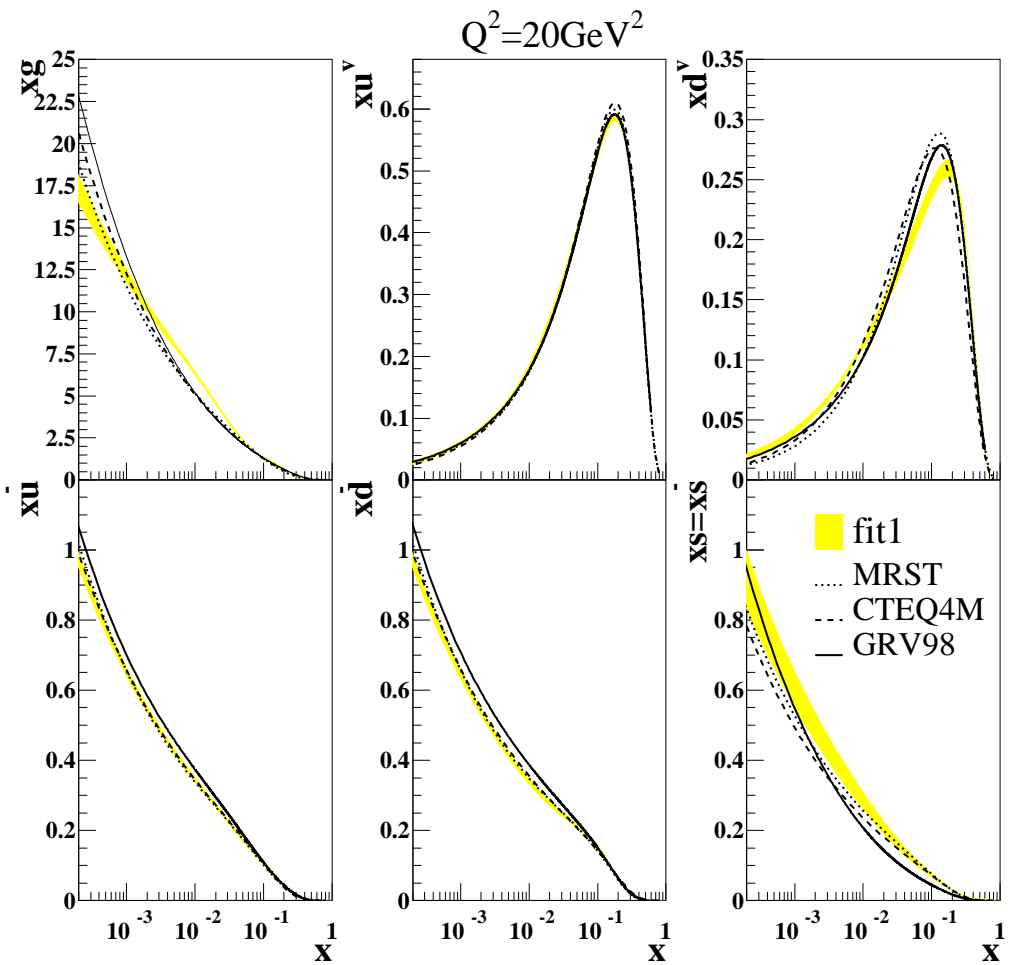


Figure 5: The parton distribution functions of **fit1**, with their error bands, compared to the GRV98 (solid line), CTEQ4M (dashed line) and MRST (dotted line) fits. The results of **fit1** for u_v , \bar{u} and \bar{d} – hardly visible – nearly coincide with the MRST and CTEQ4M results.

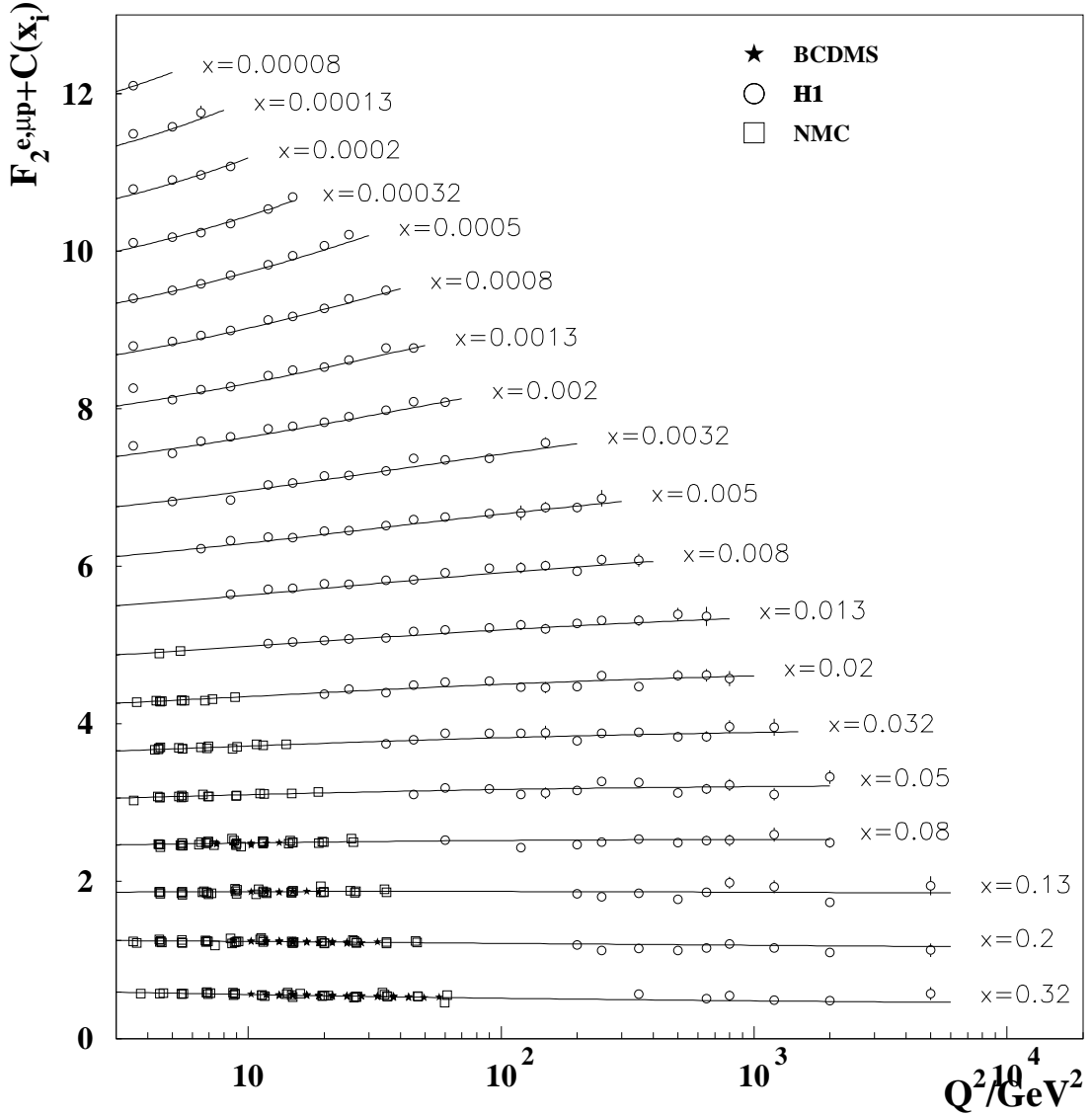


Figure 6: H1 data vs. `fit1`. BCDMS and NMC Hydrogen target data belonging to the x domain covered by H1 are also shown. These two data sets have been rebinned into the H1 x bins for plotting purpose. The data are renormalised by the overall normalisation factor determined by the fit and they are plotted with an additive bin constant $c(x_i) = 0.6 * (i - 0.5)$ corresponding to $x_i = \{0.32, \dots, 8.10^{-4}\}$. The error bars represent the quadratic sum of statistical and uncorrelated systematic errors.

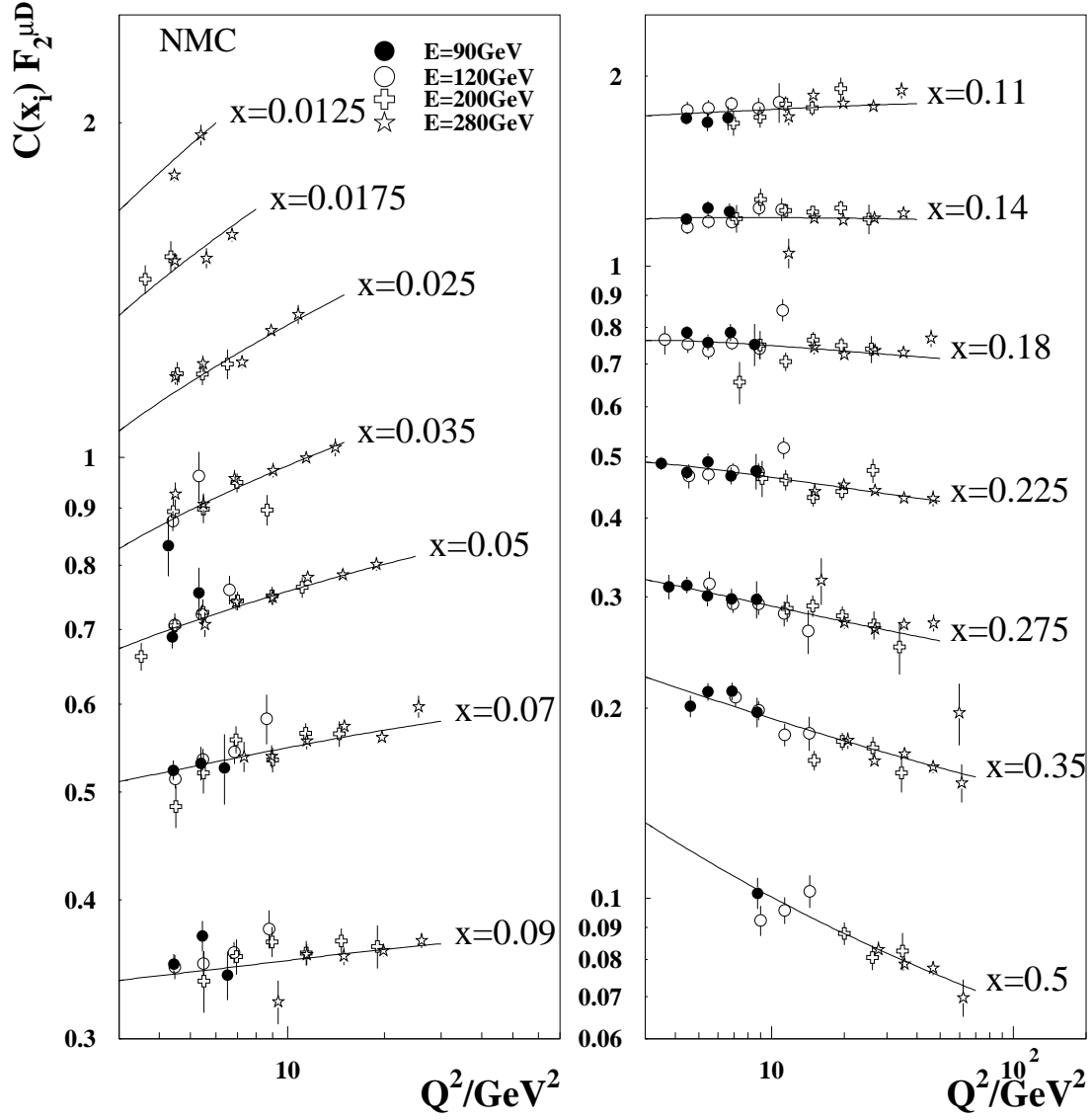


Figure 7: NMC Deuterium target data vs. `fit1`. The different beam energy samples are shown separately. The data are renormalised by the overall normalisation factor determined by the fit and multiplied by a constant $c(x_i) = \{4.8, 4, 3.2, 2.5, 2, 1.5, 1.2, 1, 7.5, 5.2, 3.7, 2.5, 1.7, 1.2, 1, 1\}$ corresponding to $x_i = \{0.0125, \dots, 0.07, 0.09, \dots, 0.5\}$. The data have been re-binned into these x_i bins for plotting purpose. The error bars represent the quadratic sum of statistical and uncorrelated systematic errors.

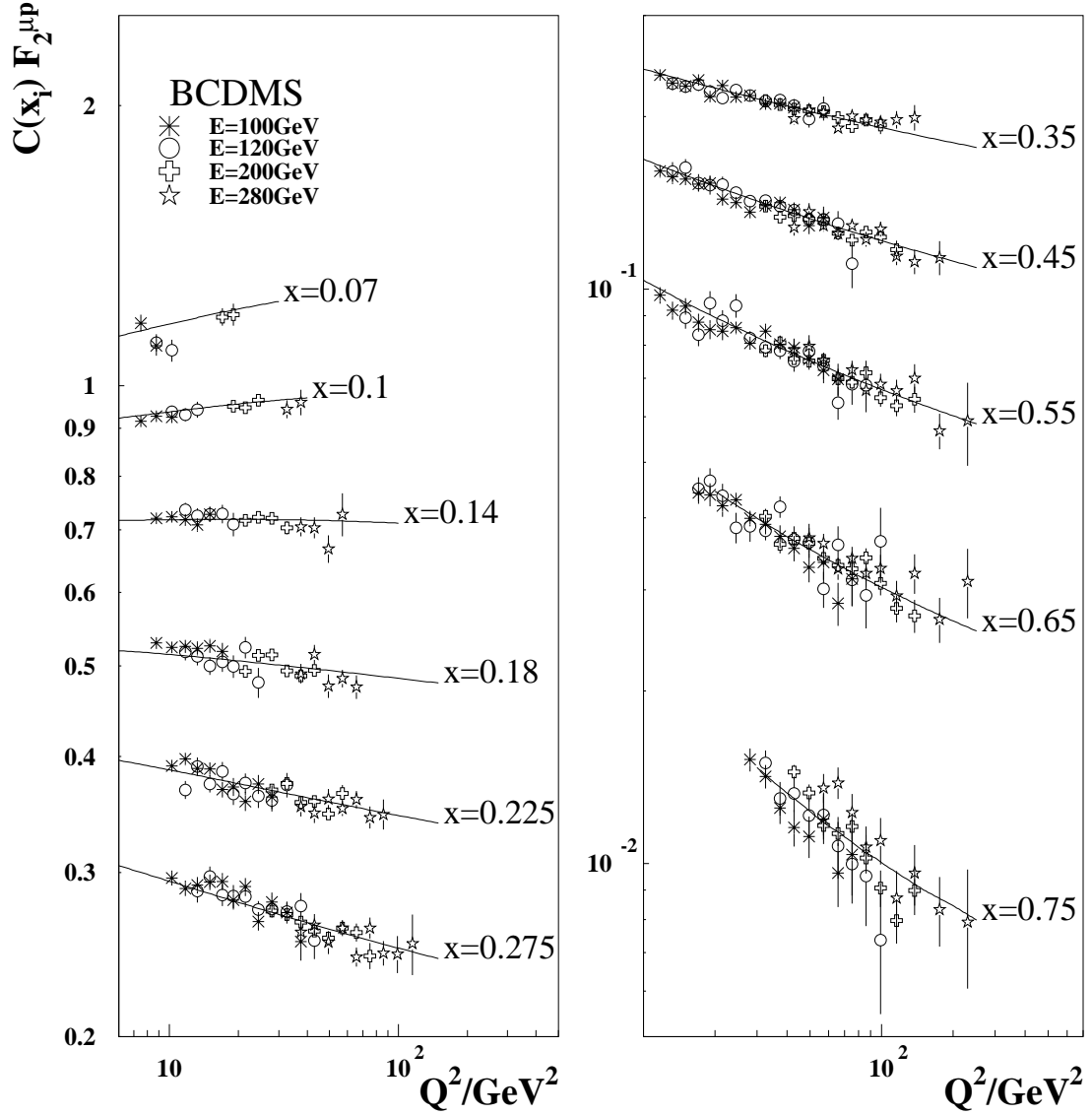


Figure 8: BCDMS hydrogen target data compared to **fit1**. The different beam energy samples are shown separately. The data are renormalised by the overall normalisation factors and the correlated systematic shifts determined by the fit. The error bars correspond to the quadratic sum of statistical and uncorrelated systematic errors. As we use the BCDMS differential cross-section data in our fits, the F_2 data shown in this plot have been determined by using F_L from **fit1**. The data are renormalised by the overall normalisation factor determined by the fit and multiplied by a constant $c(x_i) = \{3, 2.5, 2, 1.5, 1.2, 1, 1, 1, 1, 1\}$ corresponding to $x_i = \{0.07, \dots, 0.275, 0.35, \dots, 0.75\}$.

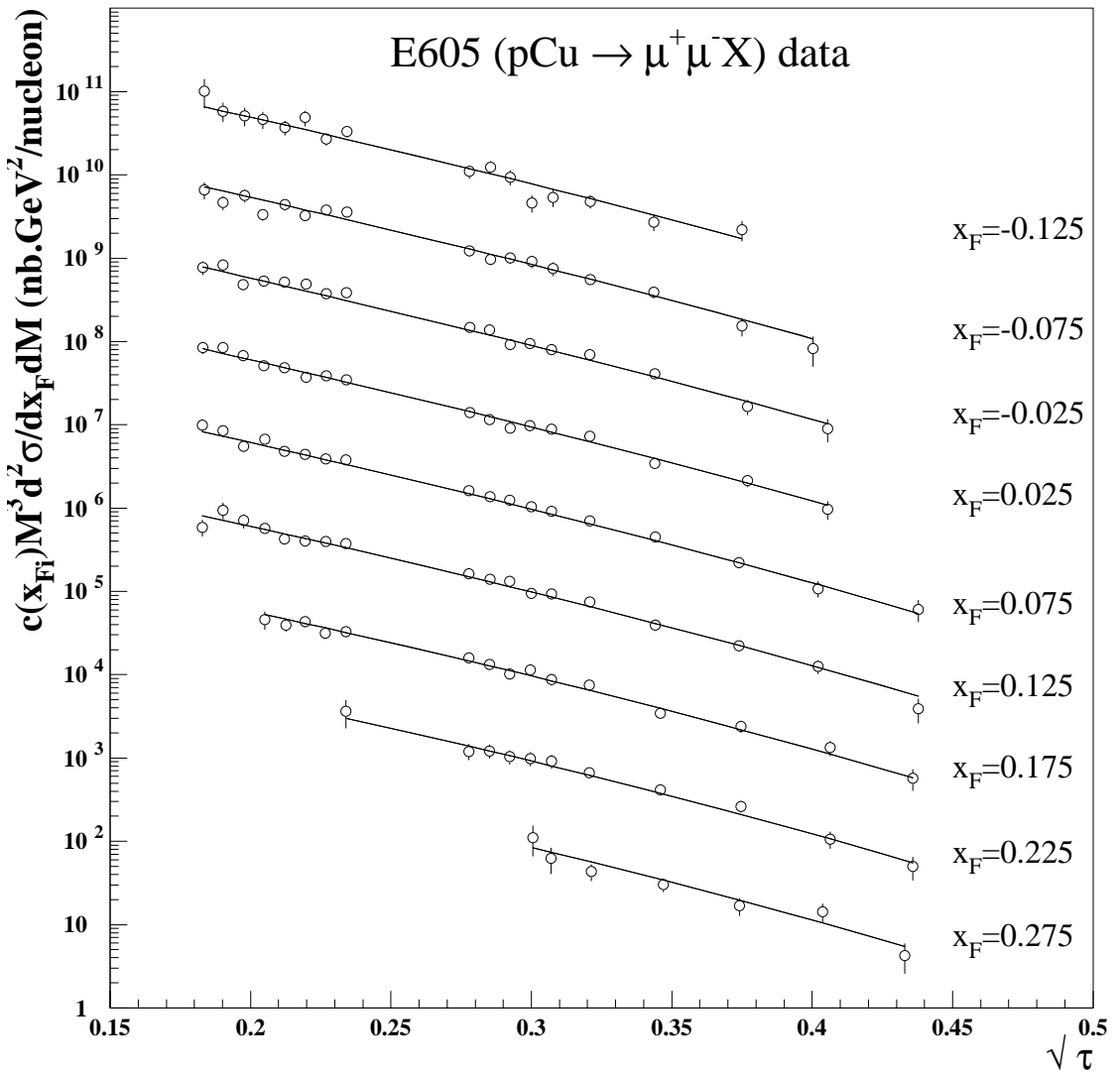


Figure 9: E605 data vs. `fit1`. The data have been renormalised by +8%, as determined by `fit1`. The data are multiplied by a constant $c(x_{Fi}) = \{10^2, \dots, 10^{10}\}$ corresponding to $x_{Fi} = \{0.275, \dots, -0.125\}$. The error bars represent the quadratic sum of statistical and systematic errors.

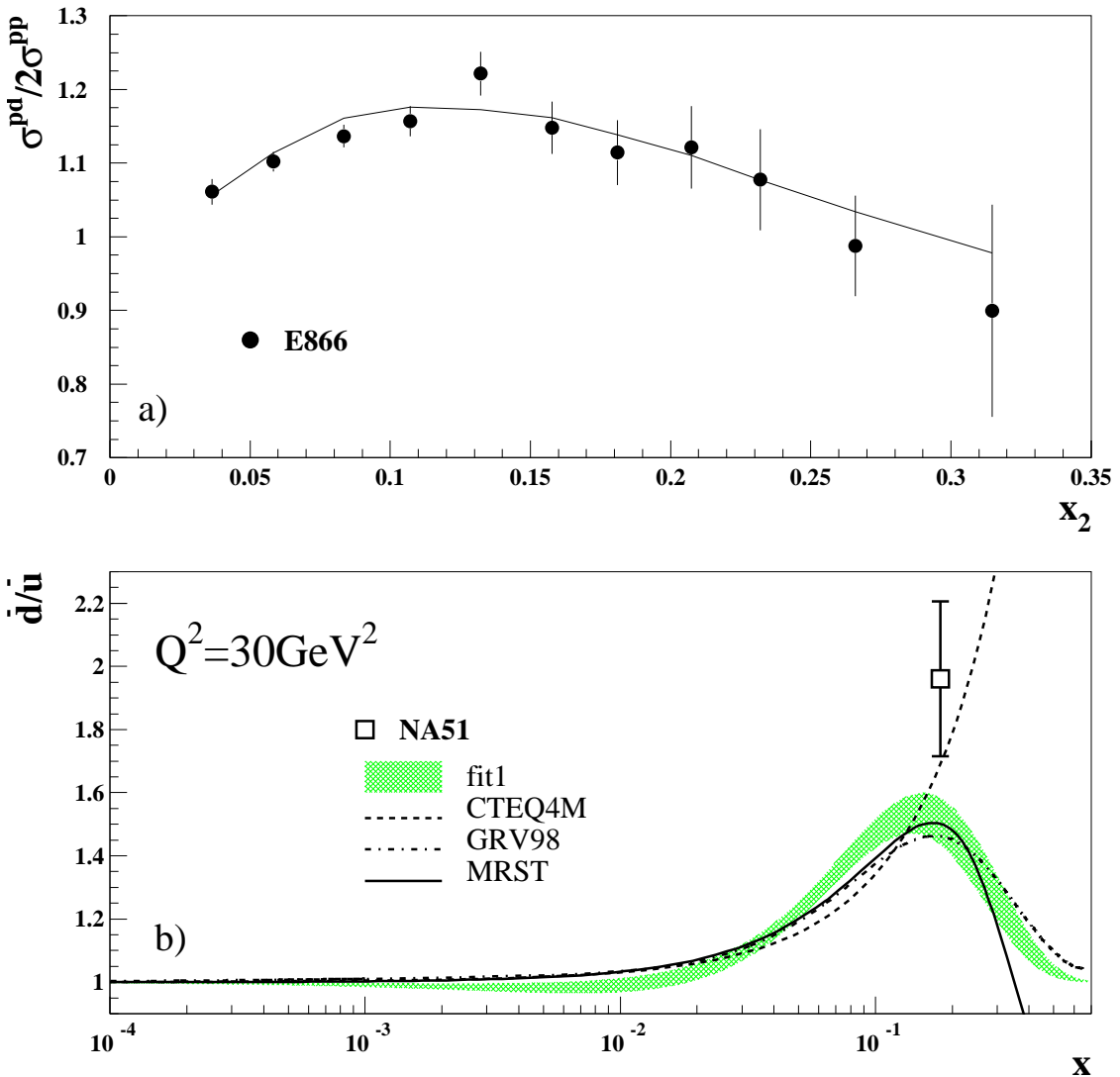


Figure 10: a) E866 vs. **fit1**. The data have been renormalised by +2% as determined in **fit1**. The error bars represent the quadratic sum of statistical and systematic errors. Notices that the data points correspond to different values of Q^2 . The line are thus an interpolation between the calculations of **fit1**. b) NA51's result for \bar{u}/\bar{d} compared to **fit1** and various parametrisations (CTEQ4M does not include the E866 data).

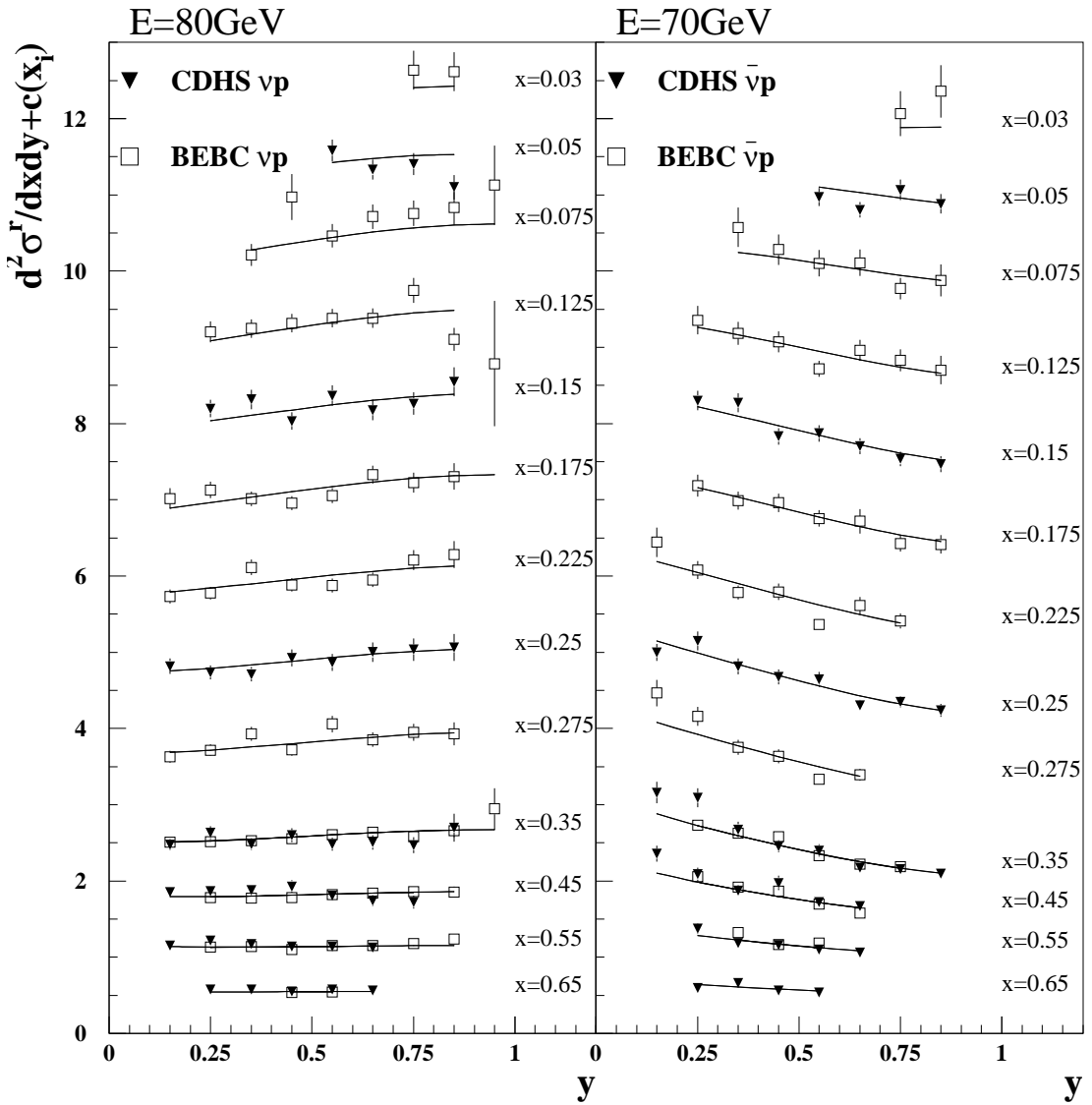


Figure 11: CDHS and BEBC Hydrogen data vs. fit1 . The BEBC data have been rebinned into the CDHS bins for plotting purpose. The data are renormalised by the overall normalisation factor determined by the fit and they are plotted with an additive bin constant $c(x_i) = \{11, 10, 9, 8, 7, 6, 5, 4, 3, 2, 1.5, 1, 0.5\}$ corresponding to $x_i = \{0.03, \dots, 0.65\}$. The error bars represent the statistical errors.

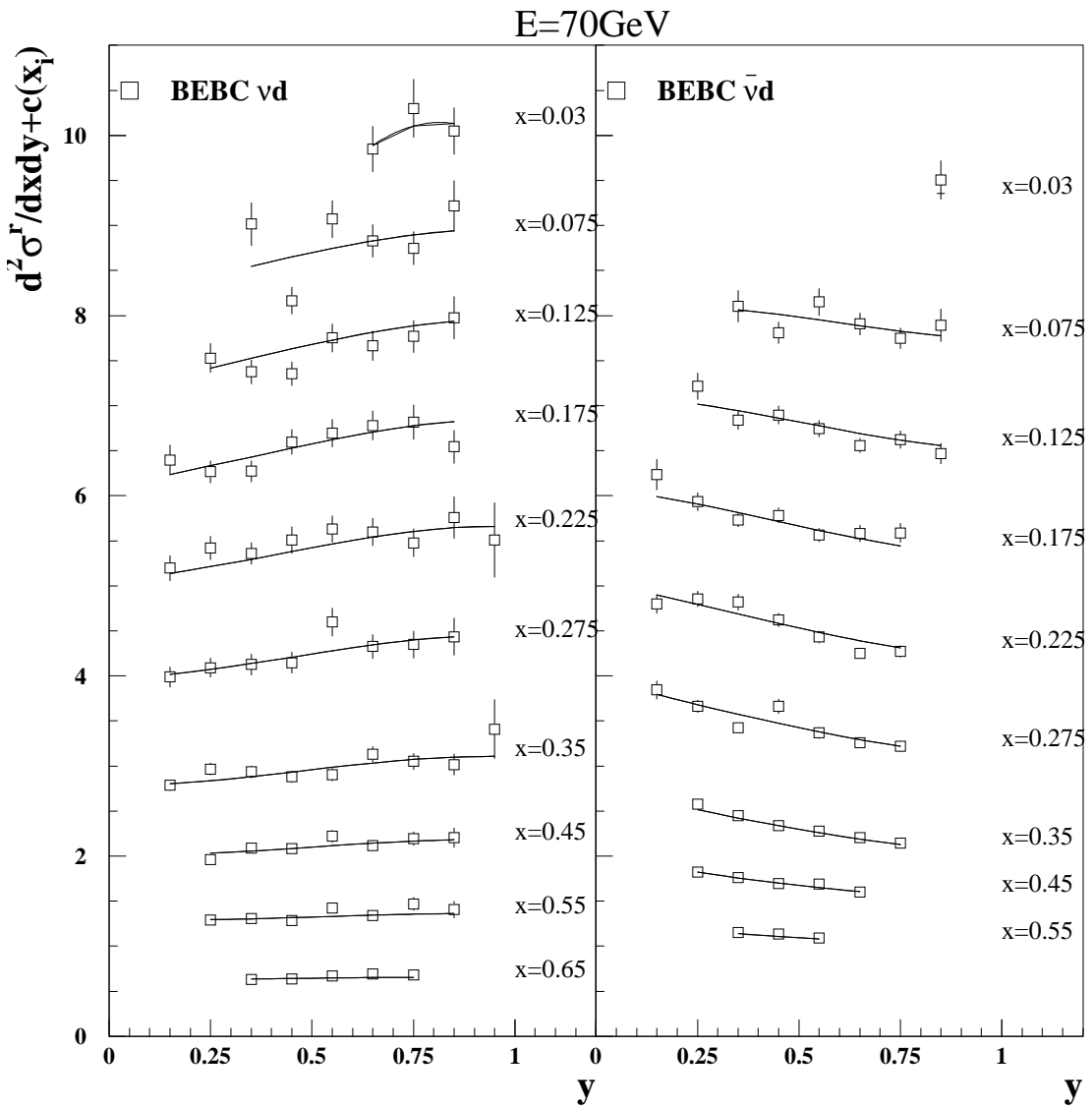


Figure 12: Same as fig. 11 but for BEBC Deuterium data. Here the additive bin constants are $c(x_i) = \{8.5, 7, 6, 5, 4, 3, 2, 1.5, 1, 0.5\}$.

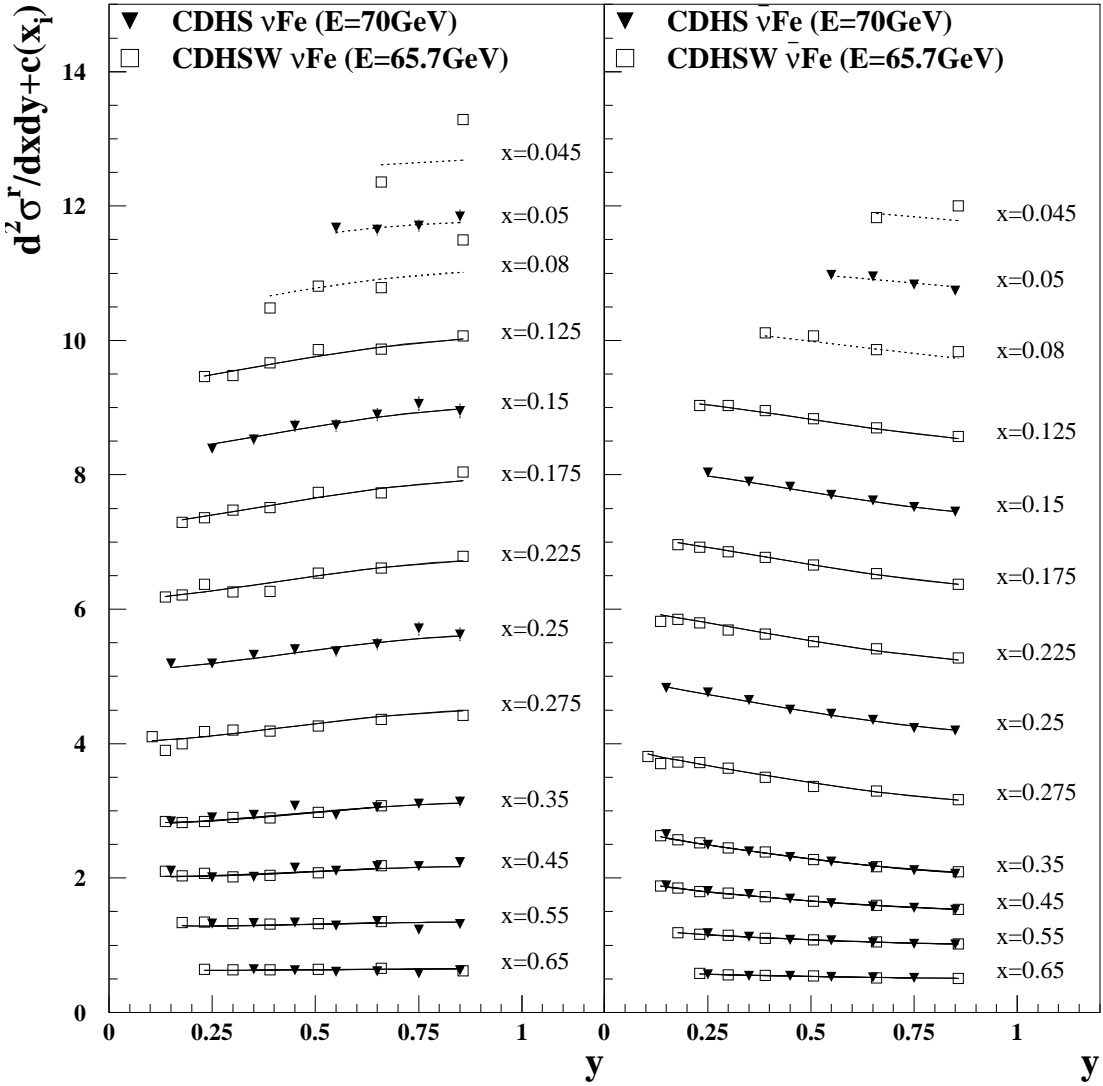


Figure 13: Same as fig. 11 but for the CDHSW 65.7 GeV beam data sample. The CDHS data ($E = 70$ GeV), though not entering the fit, are also shown. The full and dotted lines show the `fit1` results. The dotted lines describe the data rejected from `fit1` ($x < 0.1$). The nuclear correction for these particular data are taken from ref. [3]. The error bars represent the quadratic sum of statistical and uncorrelated systematic errors. The additive bin constants are $c(x_i) = \{12, 11, 10, 9, 8, 7, 6, 5, 4, 3, 2, 1.5, 1, 0.5\}$

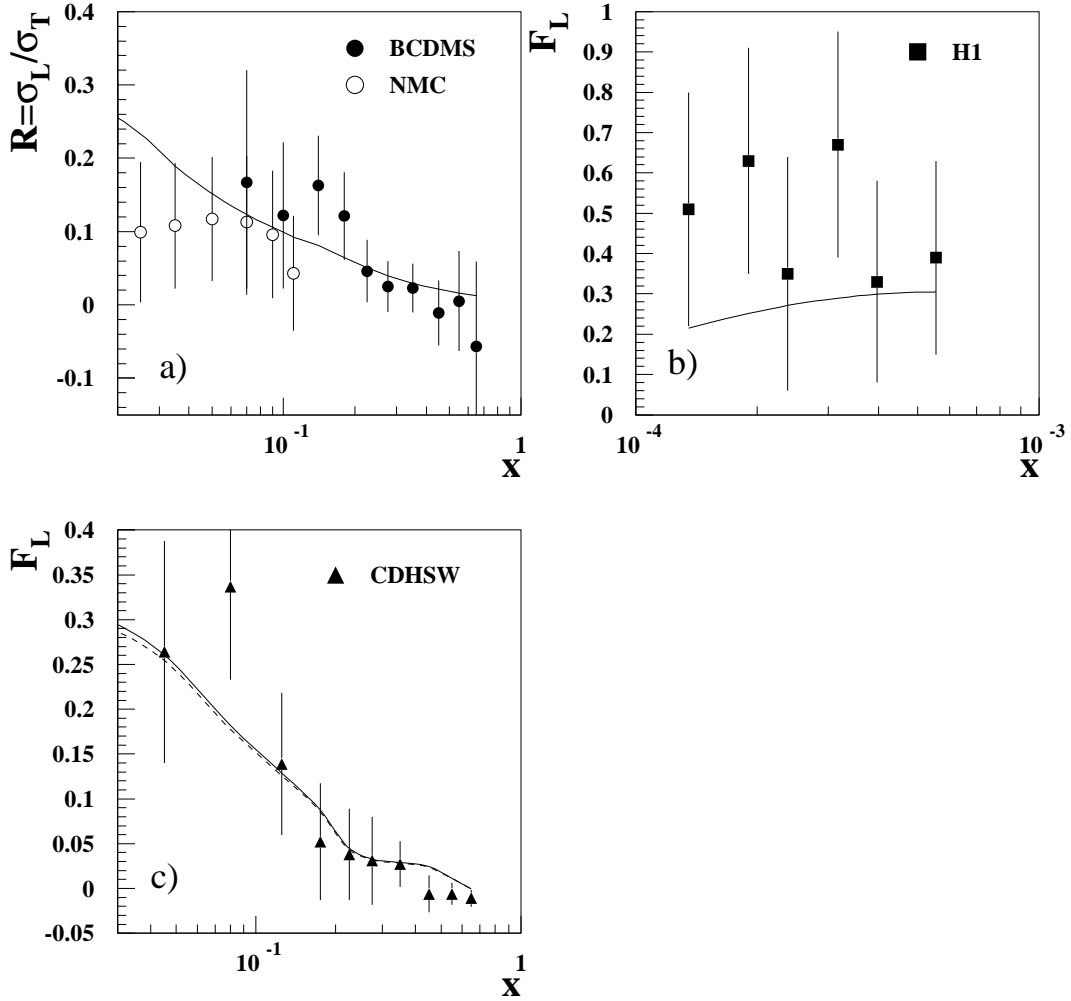


Figure 14: Results of `fit1` for the longitudinal cross sections and structure functions. Comparison of R and F_L calculated in `fit1` with: a) the BCDMS and NMC measurements of $R = \sigma_L/\sigma_T$; b) the H1 extraction of F_L ; c) the CDHSW measurements (the dashed line is F_L^ν , the solid line is $F_L^{\bar{\nu}}$). None of these measurements enter our fits and only those corresponding to $Q^2 \geq 3.5 \text{ GeV}^2$ are shown. The error bars represent the quadratic sum of the statistical and systematic errors. Each point of these plots corresponds to different values of Q^2 . The curves are obtained by interpolating smoothly between the calculations performed at these points.

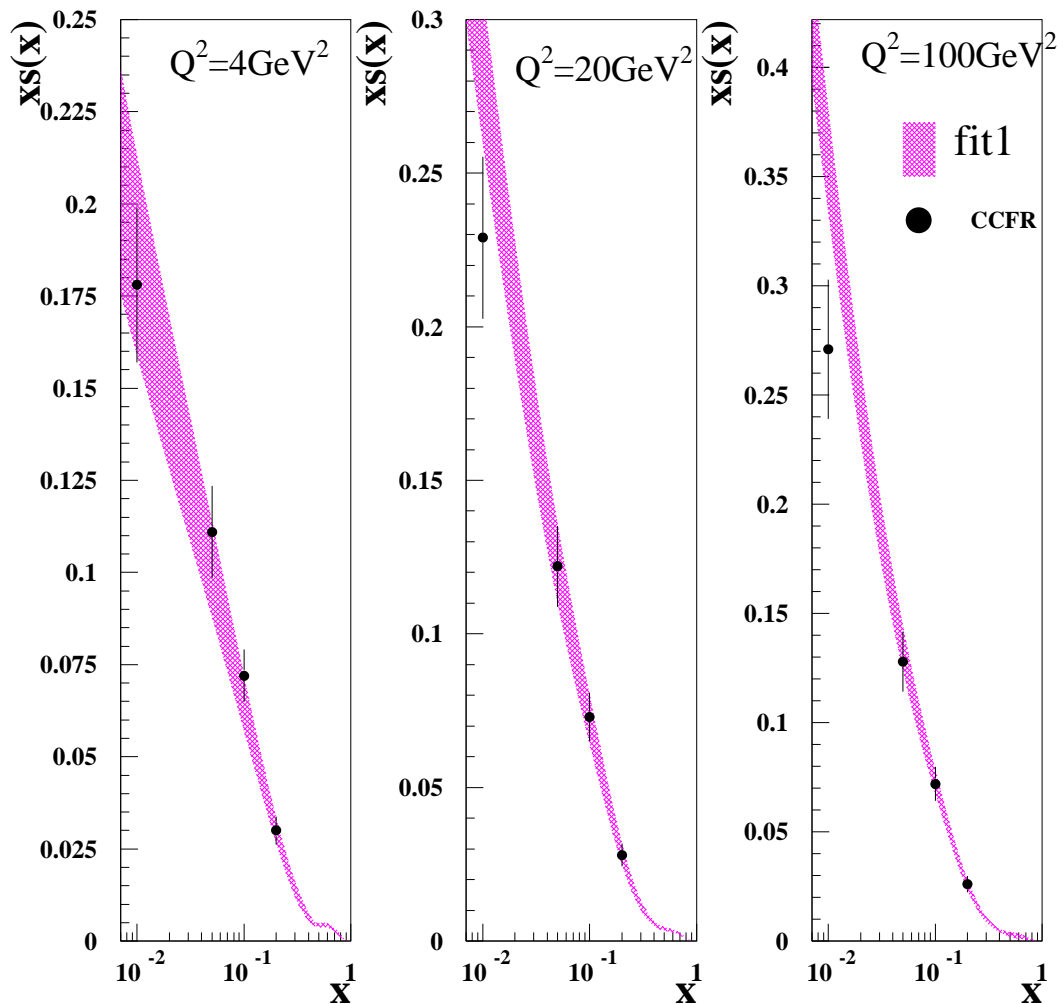


Figure 15: The strange distribution function of **fit1**, with its error band, for three different values of Q^2 . The CCFR dimuon determination (full circles with statistical and systematic errors added in quadrature) is also shown.

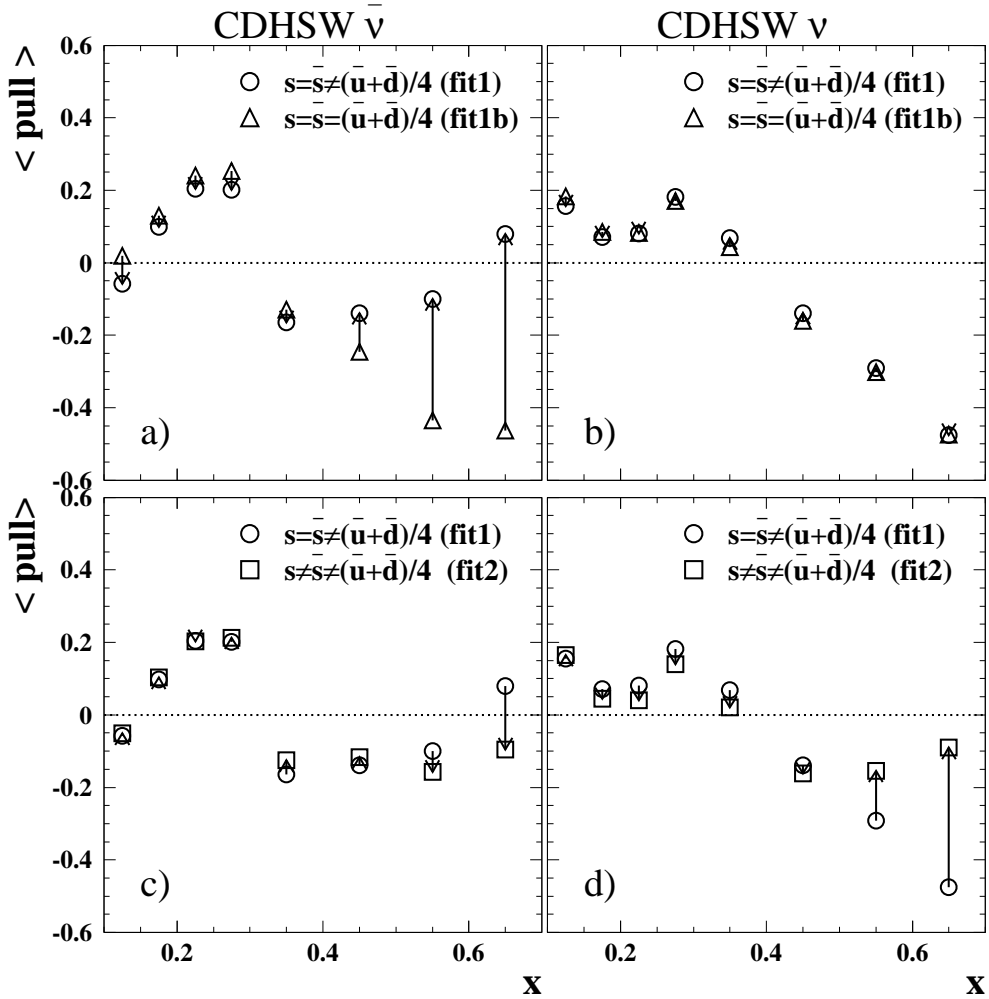


Figure 16: Mean value of the pull distribution as a function of x (see text) for CDHSW anti-neutrino (a and c) and neutrino (b and d) data. Three fits are compared (see text). The arrows describe the changes of the pull values when going from one fit to another.

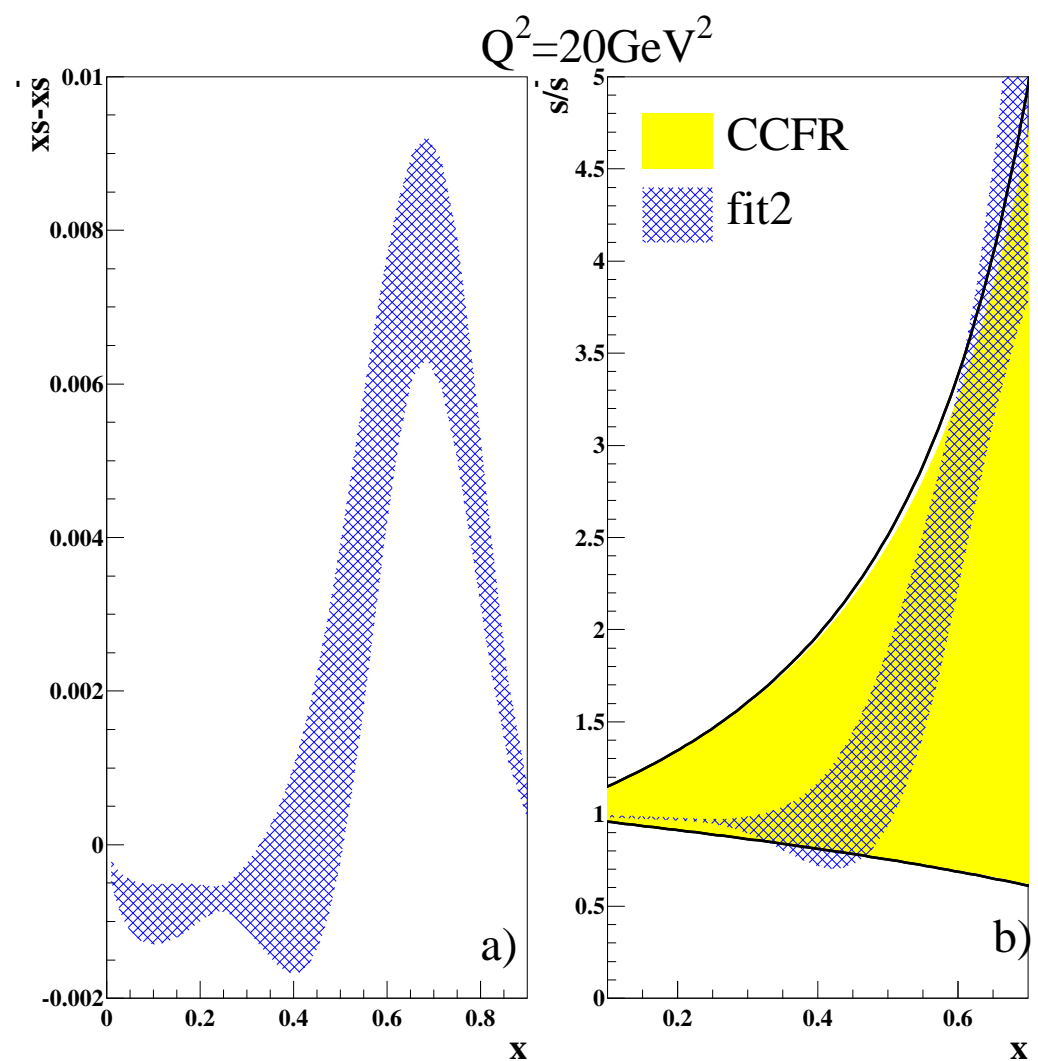


Figure 17: Results of `fit2` for: a) the difference $x(s - \bar{s})$ and b) the ratio s/\bar{s} at $Q^2 = 20 \text{ GeV}^2$. In the box b) the result of CCFR is also shown.

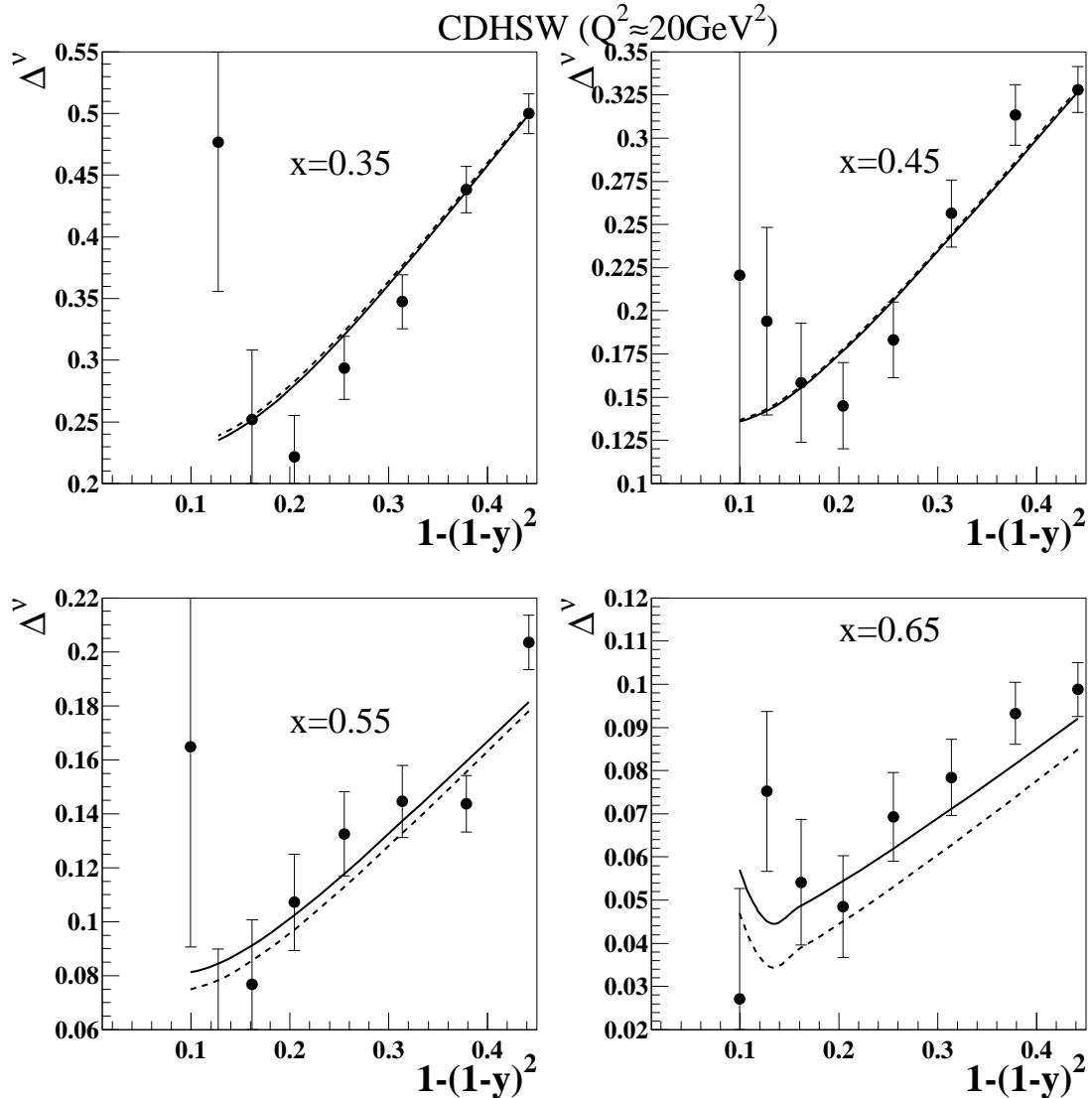


Figure 18: Difference between the νFe and $\bar{\nu} Fe$ CDHSW differential cross-sections (see eq. (36)) at fixed x and $Q^2 \approx 20 \text{ GeV}^2$ as a function of $Y_- = 1 - (1 - y)^2$. The exact values of Q^2 are 22, 21.6, 20.3, 18.6 GeV^2 for $x = 0.35, 0.45, 0.55, 0.65$, respectively.